Uplift at lithospheric swells—II: is the Cape Verde mid-plate swell supported by a lithosphere of varying mechanical strength?

D. J. Wilson,[1,*] C. Peirce,[1] A. B. Watts[2] and I. Grevemeyer[3]

[1]*Department of Earth Sciences, Durham University, South Road, Durham,* DH1 3LE*, UK. E-mail: d.j.wilson@soton.ac.uk*
[2]*Department of Earth Sciences, University of Oxford, Oxford,* OX1 3PR*, UK*
[3]*Leibniz-Institute of Marine Sciences, IFM-GEOMAR, East Shore Campus, Wischhofstr.* 1-3, D-24148 *Kiel, Germany*

SUMMARY

The Cape Verde mid-plate swell is the largest amplitude oceanic mid-plate swell on Earth at ∼1800 km in diameter, with a crest ∼2.2 km high, and long-wavelength positive geoid, gravity and heat flow anomalies of 8 m, 30 mGal and 10–15 mW m^{-2}, respectively. These characteristics and its location on the slow moving-to-stationary African Plate, which concentrates the volcanism and associated geophysical anomalies within a relatively small areal extent, makes it an ideal location to test various proposed mechanisms for swell support.

Wide-angle seismic refraction data have been acquired along a ∼474 km profile extending north–south from the swell crest. In this paper, the 2-D velocity–depth crustal model derived from forward modelling of phase traveltime picks is tested using two independent inversion approaches. The final crustal velocity–depth model derived from the combined modelling, shows no evidence for widespread thickened crust or for lower crustal velocities exceeding 7.3 km s^{-1} that are indicative of undercrustal magmatic material.

Using the final velocity–depth model to constrain the crust for 3-D 'whole plate' lithospheric flexure modelling of island loading alone, we show that the lithosphere of the Cape Verde region appears stronger than expected for its age. Regional-scale modelling suggests that the majority of the swell height is supported by dynamic upwelling within the asthenosphere coupled with, but to a lesser degree, the effect of a region of low density in the deeper lithosphere, originating most likely from conductive reheating of the overlying plate due to its slow-to-stationary motion. When this regional upward-acting buoyancy force is considered in the context of the shorter wavelength flexure associated with island loading, modelling suggests that the apparent high plate strength is a consequence of, in effect, a regional unbending of a lithosphere that has a long-term strength typical for its age.

Key words: Intraplate processes; Oceanic hotspots and intraplate volcanism; Lithospheric flexure; Crustal structure.

1 INTRODUCTION

Intraplate sites of persistent, long-term volcanic activity were initially termed 'hotspots' (Wilson 1963) due to the vast volumes of melt produced from the mantle apparently without the aid of external tectonic processes, even though they are often associated with a similar scale of volcanism to that observed at plate boundaries. Formation of hotspot-related volcanic edifices occurs either contemporaneously with crustal formation at a mid-ocean ridge axis, at a plate age of 0 Ma, or any time subsequently in a mid-plate setting as the underlying plate cools and mechanically thickens.

Intraoceanic plate seamounts and volcanoes are often observed in clusters or linear chains. Radiometric (^{40}Ar/^{39}Ar) dating of samples from ocean island basalts (e.g. Duncan & Keller 2004; Koppers *et al.* 2004; Holm *et al.* 2008) reveals that hotspot volcanism may be intermittently active for >75 Ma, often with more than 5 Ma between major eruptive phases. Some linear chains of ocean islands and seamounts, such as the Hawaiian Islands (Watts & ten Brink 1989) or the Louisville Ridge (Koppers *et al.* 2004), demonstrate a distinct age progression, and these hotspot tracks can often be traced back to large igneous provinces using records of palaeoplate motions relative to a fixed mantle hotspot reference frame (Duncan & Richards 1991).

Large volcanic island groups stand out as clear topographic anomalies in the surrounding ocean basins and exert a considerable downward-acting load on the lithosphere. Such loads must

* Now at: School of Ocean and Earth Sciences, University of Southampton, European Way, Southampton, SO14 3ZH, UK.

be supported at depth for isostatic equilibrium to be maintained. Several mechanisms have been proposed to provide additional support to surface loads or cause an upward-acting load, or buoyancy force, to counteract them. Using a standard model for the evolution of the oceanic lithosphere, it is possible to quantify surface loading and investigate how the lithosphere beneath differs when compared to 'normal' unloaded lithosphere. This, in turn, leads to an improved understanding of the long-term rheological properties of the lithosphere.

Oceanic lithosphere is created at a mid-ocean ridge following rifting and continental break-up. As thermal energy from the asthenosphere is gradually dissipated through the lithosphere, the geothermal gradient decreases, the lithosphere becomes denser and it undergoes subsidence to maintain isostatic equilibrium. A characteristic pattern of cooling and subsidence is observed, increasing with distance from the ridge axis, which can be explained by an exponential decrease in surface heat flow and an increase in bathymetry with age (Davis & Lister 1974; Sclater *et al.* 1980; Stein & Stein 1992).

As the oceanic lithosphere cools it increases its long-term mechanical strength (Watts 1978). The expected long-term (>1–2 Ma) strength of the lithosphere can be predicted from its age and the effective elastic thickness of the lithosphere (T_e) is used to express this strength numerically. The expected T_e is given by the depth of the 450 °C oceanic isotherm based on a cooling plate model (Watts 1978), although there is evidence that the controlling isotherm may vary spatially (Watts *et al.* 2006; Kalnins & Watts 2009). The apparent strength of the lithosphere can be measured by its flexural response to loading, through analysis of the amplitude and wavelength of subsidence recorded by the thickening of moat infill sediments following volcanic island construction (e.g. Watts *et al.* 1997). Unusual variation in the thermomechanical structure of the lithosphere can be detected by comparing the apparent strength of the lithosphere with the expected T_e. Measurement of lithospheric structure by seismic experiments and subsequent flexure modelling will, therefore, provide insights into the local and regional compensation of intraoceanic plate loads.

Global grids of lithospheric age (Müller *et al.* 1997, 2008), derived from the correlation of magnetic lineations to a timescale of reversals in the polarity of the Earth's magnetic field (LaBrecque *et al.* 1977; Cande & Kent 1992, 1995), have been converted to grids of predicted bathymetry using thermal models of the oceanic lithosphere. These grids have then been compared to bathymetry derived from shipboard and satellite data (e.g. GEBCO—IOC, IHO & BODC 2003). Many anomalous bathymetric highs have subsequently been identified throughout the ocean basins (e.g. Hayes 1988; Marty & Cazenave 1989) that have no apparent coherent pattern to their spatial distribution, although they commonly coincide with spatially concentrated intraoceanic plate volcanism. These highs, or swells as they are commonly called, range in size from 900 to 2000 km in diameter, with topography up to 2.2 km shallower (Monnereau & Cazenave 1990) than expected based on plate age alone (Crough 1983; Stein & Stein 1992).

Oceanic mid-plate swells are often also associated with long-wavelength gravity and geoid anomaly highs and some have excess heat flow (e.g. Crough & Jurdy 1980; Pollack *et al.* 1993), implying that the lithosphere is thermally reheated and/or mechanically weakened in some way. The magnitude and longevity of hotspot swells and their associated volcanism also indicates that they are the surface expressions of a significant melting process that may also act to dissipate excess heat from the deep interior of the Earth.

There are many factors that contribute to the size of the observed swells, including the addition of underplate material (henceforth referred to here, for clarity, as undercrustal material to distinguish its location within/beneath the crust rather than beneath the base of the lithospheric plate as the name suggests), the residence time of a region of hot asthenospheric material beneath the lithosphere and the degree of its relative elevated temperature. Such factors have been incorporated into several models of swell support that can then be tested using a range of geophysical data and modelling techniques. These models were described in detail in the first paper in this series (Wilson *et al.* 2010—fig. 1, based on Crough 1983) and so that discussion will not be repeated here. The models can be summarized as follows and it is likely that they occur in combination given observations (Monnereau & Cazenave 1990):

(1) *Shallow support within the crust* (e.g. Morgan *et al.* 1995)—volcanic island construction is often accompanied by the accumulation of neutrally buoyant magma by intrusion and emplacement at the base of the pre-existing crust (e.g. Charvis *et al.* 1999; Grevemeyer *et al.* 2001). This model also encompasses thickened crust formed due to increased magmatic activity at a hotspot-influenced mid-ocean ridge.

(2) *Support within the upper mantle* (e.g. Detrick & Crough 1978; Robinson 1988)—a region of low density in the lithospheric mantle, either due to elevated temperature or compositional variation, may provide significant upward force to elevate the lithosphere.

(3) *Dynamic mantle upwelling* (e.g. Sleep 1995)—material actively rising through the asthenosphere acts as a negative load on the base of the lithosphere and causes flexural uplift of the entire plate. Uplift may occur in two stages (Monnereau *et al.* 1993): pure dynamic support during initial ascent, and a later stage of uplift following thermal erosion of the lithosphere as the upwelling material impinges on the convective boundary layer.

In this paper, we use a model of crustal velocity–depth structure, from a transect through the Cape Verde Islands, to constrain a record of subsidence due to surface loading and to constrain crustal densities. Three-dimensional (3-D) flexure modelling is then undertaken to obtain an estimate of the apparent T_e in the region and this, together with a consideration of the long-wavelength gravity and geoid anomalies, is then used to infer the spatial and temporal mechanical properties of the lithosphere, testing the three hypotheses of swell support.

2 TECTONIC SETTING

The Cape Verde Swell is the largest amplitude mid-plate swell on Earth; the approximately circular bathymetry anomaly alone encompasses a region ~1800 km in diameter with a crest ~2.2 km shallower than the surrounding abyssal plains (Fig. 1). The slow-to-stationary absolute motion of the African Plate in the region (<10 mm yr^{-1}—Morgan 1983; Pollitz 1991) also results in a concentration of the associated uplift and volcanism into an approximately circular area and, consequently, makes this the ideal site to test the various proposed models for mid-plate swell support.

Although the crest of the swell is located only 600 km from the passive continental margin of West Africa, it is 1500 km to the nearest plate boundary, the Mid-Atlantic Ridge (MAR). The lithosphere on which the Cape Verde Islands has been emplaced is entirely oceanic, as demonstrated by the linear, ridge-parallel magnetic anomalies observed throughout the region. Magnetic anomalies M0–M21 (Hayes & Rabinowitz 1975) have been identified,
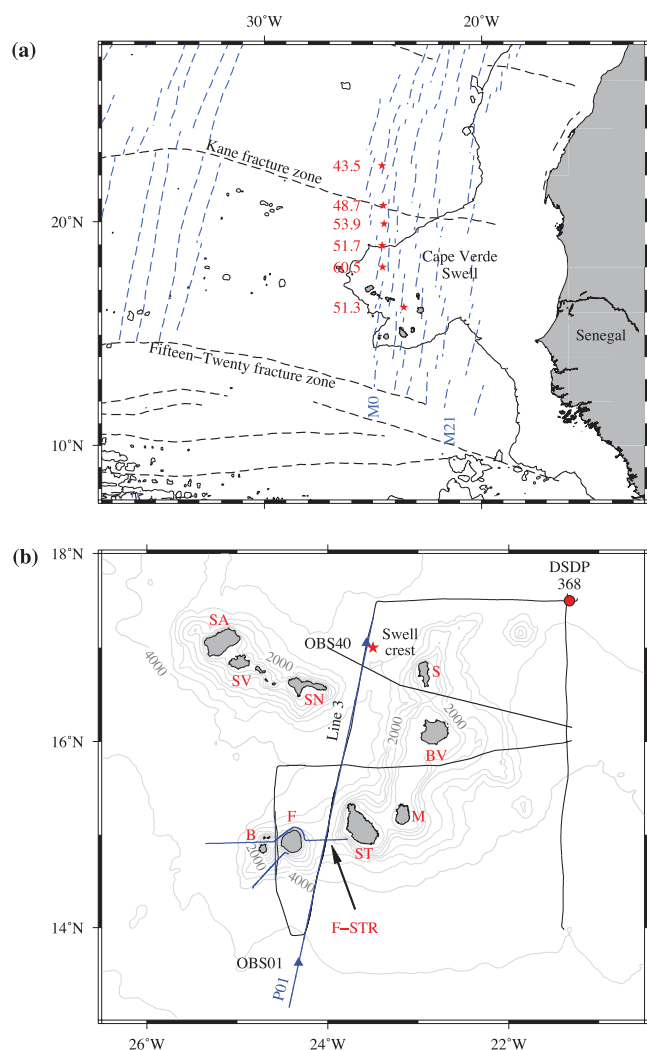
Figure 1. Tectonic setting of the Cape Verde Swell. (a) Annotated magnetic anomaly isochrons (blue dashed lines) show agreement with the plate ages of Müller *et al.* (2008) and offsets correlate with fracture zone locations (black dashed lines). Courtney & White's (1986) heat flow measurements, in mW m^{-2} (red stars and text) show a positive heat flow anomaly over the swell. The 4000-m bathymetric contour (solid black line) shows the extent of the swell adjacent to the West African continental margin. (b) The Cape Verde archipelago with the swell crest marked by the red star and DSDP site 368 by the red dot. Bathymetric contours are plotted at 500 m intervals and highlight the islands of Santo Antão (SA), São Vicente (SV), São Nicolau (SN), Sal (S), Boa Vista (BV), Maio (M), Santiago (ST), Fogo (F) and Brava (B) and the Fogo-Santiago Ridge (F–STR). The blue lines mark seismic profiles acquired during 'R/V Meteor' M62/3 (Grevemeyer *et al.* 2004), with the swell transect profile (P01) annotated together with the end of profile ocean-bottom seismographs (numbers 1 & 40—blue triangles; Wilson *et al.* 2010). Black lines show multichannel seismic profiles acquired during 'RRS Charles Darwin' CD8/85 (Ali *et al.* 2003).

which are offset by several large fracture zones (Williams *et al.* 1990; fig. 1) that accommodated the separation of the African continent from the Americas in the early Cretaceous (Berriasian to Albian, ~150–110 Ma). The regional geoid anomaly reaches a maximum of +8 m (Monnereau & Cazenave 1990) and heat flow measurements show an increase from 43.5 mW m^{-2} away from the swell, to 60.5 mW m^{-2} near the swell crest (Courtney & White 1986; fig. 1). The maximum heat flow anomaly is 16 mW m^{-2} higher than predicted for the regional average 130 Myr old, oceanic lithosphere

on which the swell is imposed, and assuming the thermal cooling plate model of Parsons & Sclater (1977).

The age of swell formation is uncertain. Stillman *et al.* (1982) suggest from outcrops of Jurassic age mid-oceanic ridge pillow lavas on Maio, that a localized rapid shallowing and emergence began as early as the Albian. A study of the concentration of carbonate nannofossils in cores from Deep Sea Drilling Program (DSDP) site 368 (Lancelot *et al.* 1978b) located on the swell crest, in comparison to those from DSDP Site 367 (Lancelot *et al.* 1978a) in the basin to the south, reveals a sudden increase in abundance between the lower and upper Miocene. Assuming that there has not been a dramatic change in nutrient availability or palaeoclimate in this region at that time, this would suggest a regional shallowing of the seabed above the carbonate compensation depth by ~20 Ma, although it is not impossible that the carbonate compensation depth alternatively changed due to climatic factors. Finally, evidence from observations of wave-cut surfaces, marine terraces and lava deltas on São Nicolau and Santiago (Ramalho *et al.* 2010) suggest up to ~450 m of regional uplift during the past 6 Myr.

The Cape Verde archipelago is centred to the southwest of the swell crest and consists of nine main islands, clustered in a circular area ~350 km in diameter, that can be subdivided into a crescent of six islands to the southeast and a chain of three aligned towards the northwest (Fig. 1). The Cape Verde Islands are composed of plutonic intrusions, a series of extrusive sequences, and volcaniclastic and mass wasting volcanic deposits. Seabed imaging also suggests that the intraisland regions of the volcanic edifice, such as the Fogo-Santiago Ridge (F-STR), are also predominantly covered with island mass wasting debris flows (Day *et al.* 1999; Masson *et al.* 2008). In some cases, there is evidence of uplifted marine sediments, predominantly comprising carbonates that predate the island building volcanism. The islands were all constructed in the last ~20 Myr (Holm *et al.* 2008 and references therein), and the volcanism appears to have occurred in three to four periods with overlapping time frames: the oldest islands of Sal, Boa Vista and Maio in the east (≤20.0 Myr old); the intermediate islands of Santo Antão, São Vicente and São Nicolau to the northwest (≤7.5 Myr old); the young island of Santiago to the south (≤4.6 Myr old), with the possible distinction of the most recent volcanism at the islands of Fogo and Brava in the southwest (≤3.0 Myr old).

3 CRUSTAL MODEL AND MODEL RESOLUTION

A variety of marine geophysical data have been analysed to investigate the shallow and deep structure of the Cape Verde region. Full details of the seismic data acquisition along the interisland/swell transect (profile P01—Fig. 1) conducted during 'R/V Meteor' cruise M62/3 (Grevemeyer *et al.* 2004), and the other marine geophysical data used to derive the models discussed in this paper, can be found in Pim *et al.* (2008), Ali *et al.* (2003), Wilson *et al.* (2010) and Wilson (2011).

The 3-D flexural modelling presented in this paper requires knowledge of the underlying crustal structure and the volume and extent of the lithospheric load (e.g. volume and density of undercrustal material, the islands and the sediment infill in the island moats). These can be determined directly from, or may be constrained by, the velocity–depth model derived primarily from modelling of the wide-angle (WA) seismic data acquired during 'R/V Meteor' cruise M62/3 (Pim *et al.* 2008; Wilson *et al.* 2010). Calculating the regional gravity field of the flexure model also provides

a means of estimating crustal thickness beneath each island which, in turn, can be compared to 1-D structural models derived from receiver function analysis of teleseismic recordings made on a number of the islands (Lodge & Helffrich 2006).

Prior to flexural modelling it is, therefore, important to first determine if the swell transect profile (P01) velocity–depth model is sensitive to the scale of features required, or resolvable by the flexural modelling approach adopted. It is also important to check that there is no inherent modeller bias, in terms of pre-conceived structures and velocities, built into the model by the forward approach. The latter is particularly important since model velocities are used not only for time-to-depth conversion of sediment load isochron maps derived from multichannel seismic (MCS) data ('RRS Charles Darwin' cruise CD8/85—Ali *et al.* 2003), but also to determine the density to be used for the flexural load modelling itself.

Two modeller-independent inversion approaches, *FAST* (Zelt 1998) and *tomo2d* (Korenaga *et al.* 2000), were used to assess the resolution and sensitivity of the crustal model derived using the forward modelling, *rayinvr,* approach (henceforth referred to as the *rayinvr* model—Zelt & Smith 1992). In addition to providing a means of assessing the degree of modeller-induced bias, independently inverting the observed phase traveltime picks also allows assessment of the accuracy to which structures incorporated into the *rayinvr* modelling (Fig. 2) are replicated by each of the inversion

methods. The degree to which structures and velocity anomalies in the inversion models match the *rayinvr* model, both in terms of depth and lateral variation [mismatch between specified model boundaries (*rayinvr* model) and matching velocity contours (inversion-derived models)], is used to define the resolution and error bounds on the input density and depth parameters for 3-D flexural modelling. The depth to and geometry of the Moho, in particular, were investigated, as ray coverage at lower crustal and upper-mantle depth is limited.

3.1 *FAST*

The *FAST* programme uses a regularized framework of grid nodes to define a model, and a grid node spacing of 0.1 km in both the *x*- and *z*-dimensions was chosen to, primarily, avoid spatial aliasing given the average shot spacing of 0.18 km. During inversion, updates to the velocity field were applied on a larger scale than the maximum resolution of the data, again avoiding spatial aliasing, using cells measuring 2.0 km in the *x*-dimension and 0.4 km in the *z*-dimension. Smoothing and damping parameter choices were based on the approach adopted by Zelt & Barton (1998) where *FAST* was applied to a 3-D data set in an oceanic setting. As *FAST* is unable to model reflections, inversions were limited to incorporating first-arrival traveltime picks only, corresponding to the shallow
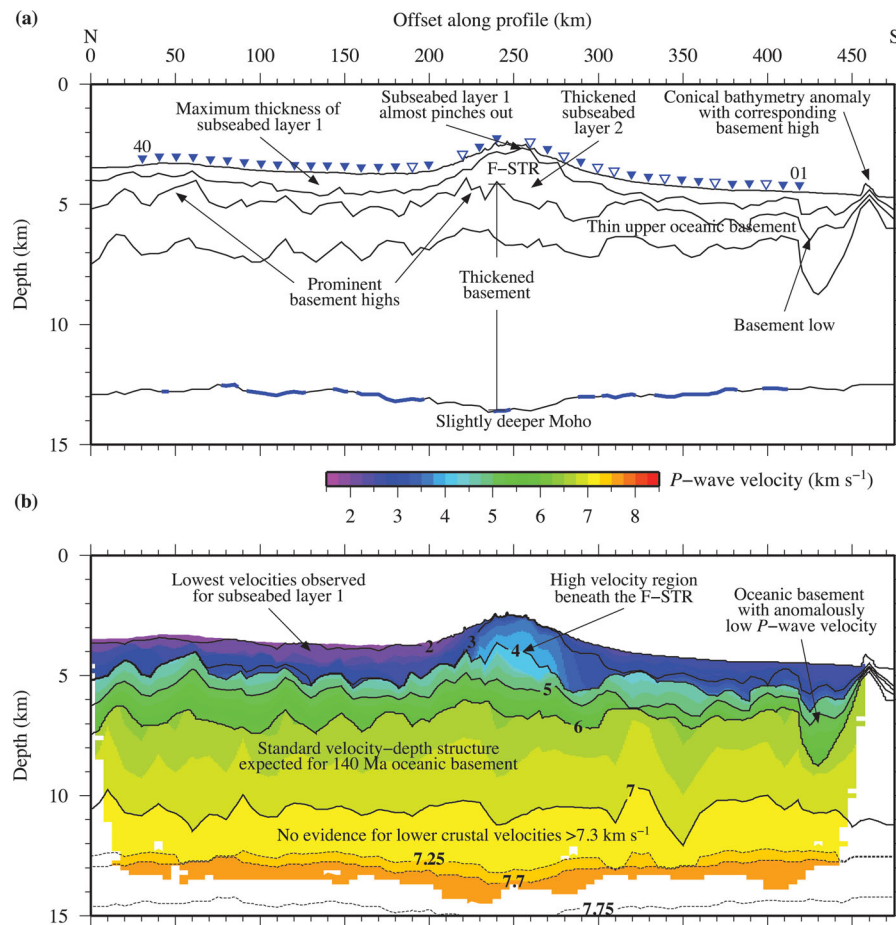
Figure 2. Layer and 2-D velocity–depth structure of the *rayinvr* model. (a) The boundary surfaces of the model are shown (black lines). Blue shading on the Moho indicates the regions constrained by P_mP arrivals. Key structures, described in Wilson *et al.* (2010), are annotated. (b) The 2-D velocity–depth structure of the *rayinvr* model. *P*-wave velocity coloured shading is masked to show the extent of ray coverage. Isovelocity contours (black lines) are plotted with a 1 km s^{-1} contour interval. The 7.25, 7.7 and 7.75 km s^{-1} contours (black dashed lines) highlight the velocity structure of the lower oceanic basement and uppermost mantle.
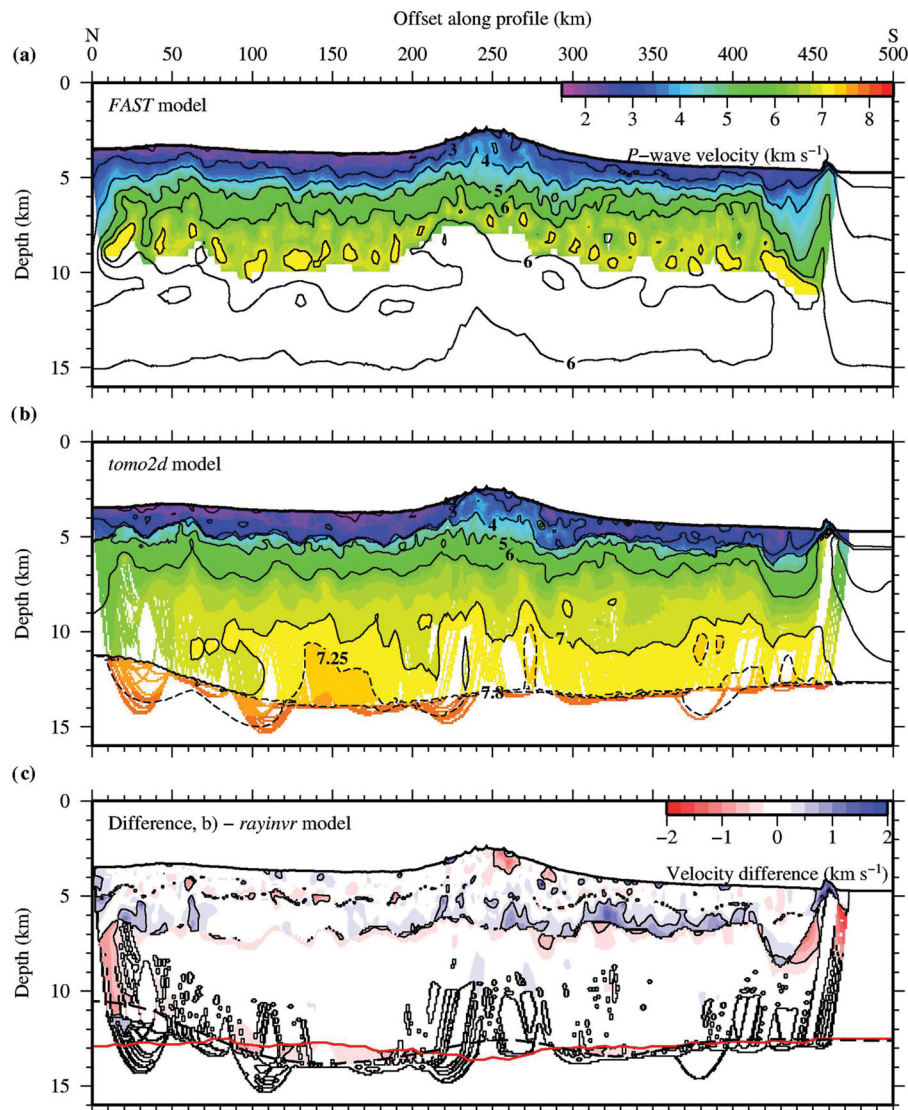
Figure 3. Velocity–depth models resulting from inversions with (a) *FAST* and (b) *tomo2d*. *P*-wave velocity coloured shading is masked to show the extent of ray coverage. Isovelocity contours (black lines) are plotted with a 1 km s^{-1} contour interval. The 7.25 and 7.8 km s^{-1} contours in (b) (black dashed lines) highlight the velocity structure of the lower oceanic basement and uppermost mantle. (c) Difference between the *rayinvr* model and the *tomo2d* model. The red and black dashed lines show the location of the Moho following modelling with *rayinvr* and inversion with *tomo2d*, respectively. Velocity difference contours are included (black lines) at ±0.5 km s^{-1} intervals to highlight areas of significant mismatch. See text for discussion.

subseabed (P_s) and crustal (P_{g1} and P_{g2}) phases. This method is, therefore, limited to resolving the velocity structure down to mid-to-lower crustal depths only given the paucity of upper-mantle (P_n) arrivals.

Preliminary synthetic inversions were first used to test the subseabed imaging potential and the influence of the starting model. Synthetic traveltime data, with the same spatial distribution as the observed, were generated by forward ray tracing through the *rayinvr* model and a component of random noise was added. With the aim of introducing no model bias, a simple two-layer starting model with a pseudo-1-D velocity–depth structure, defining the water column and the subseabed, was constructed. Synthetic inversion of this starting model resulted in only a shallow maximum depth of penetration (8.0 km b.s.l.), a result of overcorrection for the low velocities of the shallowest subseabed.

To increase the maximum depth of ray coverage, and thereby improve the model recovered by the inversion, constraints had to be placed on the shallow subseabed. Since the shallow subseabed

structure of the *rayinvr* model has been independently tested, using the depth-to-time conversion of its mid-sediment and top-basement layer boundaries and their comparison with the corresponding events in the available 'RRS Charles Darwin' CD8/85 MCS reflection data (Ali *et al.* 2003; Wilson *et al.* 2010), a revised starting model was constructed with a 2-D velocity–depth structure down to the top-basement surface, beneath which the velocities were then set to increase linearly to 7.5 km s^{-1} at the base of the model, 20 km b.s.l. Synthetic inversion of this 2-D starting model produced turning rays to a depth of 8.75 km b.s.l., and although the input model did include a degree of modeller-introduced bias, it had little effect on the final result other than improving the imaging potential of the inversion (i.e. depth to which anomalies could reliably be recovered—Wilson 2011).

The output model from the inversion using the real traveltime picks (henceforth referred to as the *FAST* model—Fig. 3a), resembles the *rayinvr* model (Fig. 2) within the lateral confidence/resolution boundaries of that approach, and the velocity–
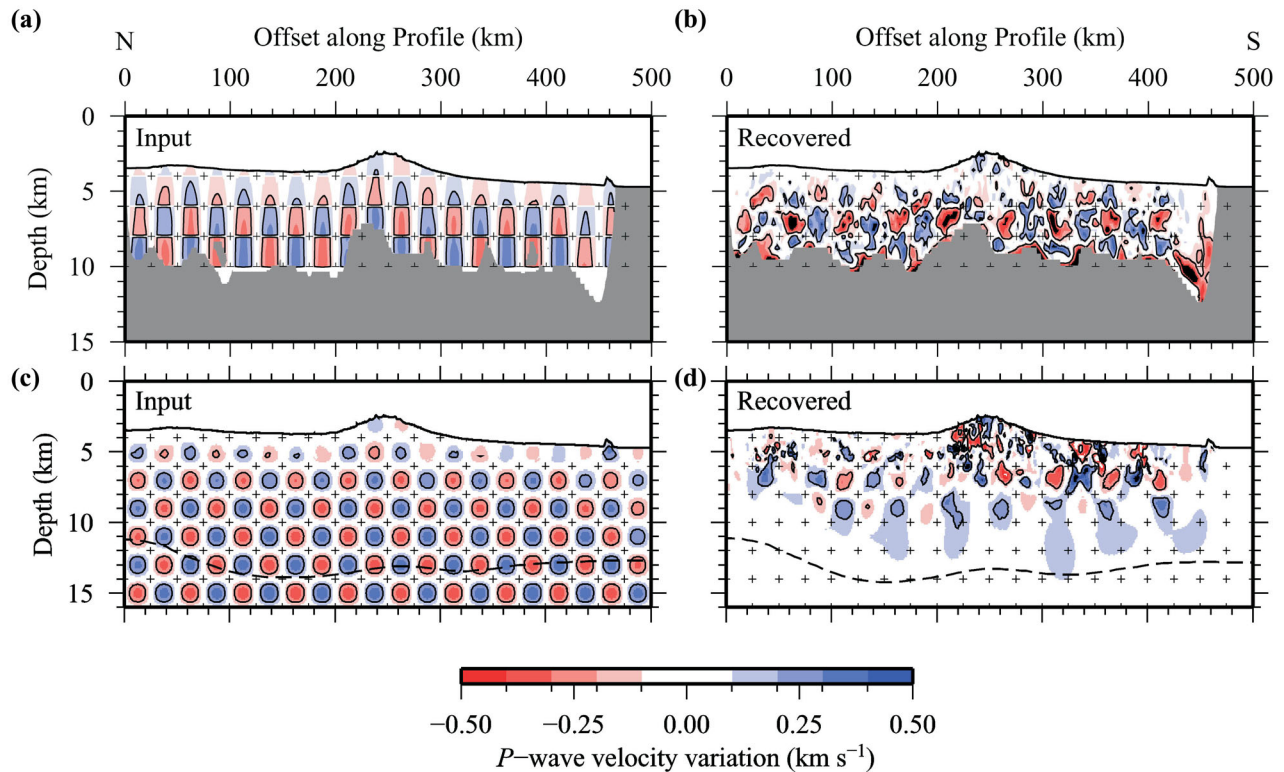
Figure 4. Resolution testing of the *FAST* and *tomo2d* approaches using a checkerboard anomaly pattern below the seabed. (a) and (b) The *FAST* approach with an input checkerboard size of 25 by 2 km and maximum anomaly amplitudes of ± 5 per cent (a) is compared to the anomaly recovered by the inversion process (b). (c) and (d) The *tomo2d* approach with an input checkerboard size of 25 by 2 km and maximum anomaly amplitudes of ± 5 per cent (c) is compared to the anomaly recovered by the inversion process (d). Black dashed line shows the initial and final locations of the Moho reflector. Black crosses in parts (b) and (d) highlight the corners of the checkerboard regions and anomalies are contoured at 0.2 km s^{-1}.

depth structure closely resembles that of mature Atlantic oceanic crust (White *et al.* 1992). Checkerboard testing over a range of scales (Wilson 2011) defined the horizontal and vertical resolution limits of the *FAST* model to be 25 and 2 km, respectively, with amplitude perturbations of ± 5 per cent still resolvable (Figs 4a and b).

3.2 *tomo2d*

The *tomo2d* programme uses a 'hanging mesh' model to define nodal positions, whereby horizontal gridlines follow the bathymetry. A regular mesh was chosen with grid node intervals of 1.0 km in both the *x*- and *z*-dimensions, with nodes extending to a maximum depth of 15 km below the seabed. Although the inversion step works on the same mesh, smoothing parameters are defined to prevent incorporation of velocity anomalies below the spatial resolution of the data. The horizontal smoothing lengths increased linearly from 1.5 km directly beneath the seabed to 15.0 km at the base of the mesh. Similarly, the vertical smoothing lengths increased from 0.15 to 1.5 km.

As with *FAST*, preliminary synthetic inversions were conducted with *tomo2d* to test imaging potential and starting model suitability. Synthetic inversion of the 2-D starting model used for the *FAST* inversions resulted in areas of unrealistically low *P*-wave velocities (<1.5 km s^{-1}) in the shallow subseabed. Similarly, the high-velocity region beneath the F-STR in the *rayinvr* model was not accurately reproduced. As the uppermost section of the model is already well constrained by the MCS reflection data (Wilson *et al.*

2010), and supported by the results from the *FAST* inversion, a revised starting model was created to suppress the production of areas of unrealistically low velocity in the shallow subseabed. The revised starting model differs from the original 2-D model only from the top-basement boundary downwards, where the velocity now increases from 4.5 to 8.3 km s^{-1} at the base of the model (20 km b.s.l.). Synthetic inversion with the revised 2-D starting model resulted in an output model that did not include any unreasonably low-velocity areas and demonstrated improved ray coverage throughout (Wilson 2011).

Subsequently, the Moho reflection (P_mP) phase traveltime picks were incorporated into a joint inversion of both the velocity structure and a reflection-generating boundary, which is hereafter referred to as a reflector. Synthetic inversion resulted in excellent recovery of both the velocity–depth structure between 20- and 430 km profile offset, and of the Moho reflector between 70- and 380 km profile offset, even beneath the F-STR where there is significantly reduced ray coverage (Fig. 3b; Wilson 2011).

This inversion demonstrated that *tomo2d* requires a significant degree of modeller input, especially when compared to *FAST*, to produce a model that fits any traveltime data. However, given that *FAST* is limited to inversions that use only first-arrival traveltime data, the application of *tomo2d* to a model with pre-constrained shallow subseabed structure is a realistic test of modeller independence, especially in this case where it is necessary to assess the Moho depth and sub-Moho velocities obtained using the forward modelling approach given the sparse ray coverage at these depths.

A total of three *tomo2d* inversions were made using the observed traveltime data. Two of these inversions used the revised 2-D model

as a starting point, with the first incorporating traveltime picks from the P_s, P_{g1} and P_{g2} phases to produce an output model directly comparable to the result of the *FAST* inversion. The second included traveltime picks from the P_mP phase to produce a model constrained down to the Moho reflector. The final inversion started with the output model from the second inversion and incorporated traveltime picks from the P_n phase to recover the velocity structure of the uppermost mantle.

The output model (Fig. 3b), henceforth referred to as the *tomo2d* model, is very similar to the result of the *FAST* inversion (Fig. 3a), but is smoother at maximum ray coverage depth. Analysis of the difference between the *rayinvr* model and the *tomo2d* model (Fig. 3c) shows velocities that agree to within 0.25 km s^{-1} except immediately adjacent to the *rayinvr* model layer boundaries and the regions of overlap between the two contrasting Moho solutions. The *tomo2d* model is better constrained than the *FAST* model due to the increased ray coverage at mid-to-lower crustal depths and the broader range of phase traveltime picks incorporated. The average velocity of the uppermost mantle in the *tomo2d* model is 7.8 km s^{-1}, which agrees with the *rayinvr* model (7.7 km s^{-1}) to within the uncertainties. The vertical velocity gradient in the mantle ranges from 0.03 to 0.04 s^{-1} (Fig. 3b), which is significantly smaller than the gradient in the *rayinvr* model (0.11 s^{-1}). This large difference most likely arises from differences in Moho geometry and, because the shallow depth of penetration of P_n ray paths beneath the Moho provides only limited constraint, the vertical velocity gradients derived from both the forward modelling and the inversion remain largely uncertain.

Given that the *rayinvr* and *tomo2d* approaches create models with limited resolution in both velocity and geometry at Moho depths, and given that the geometry and depth of the Moho is a key input parameter for the 3-D flexural modelling, a series of checkerboard tests such as those undertaken for the *FAST* model, were also undertaken. A similar result was achieved—that is, horizontal and vertical resolution limits of the *tomo2d* approach were also 25 and 2 km, respectively, with a resolvable velocity anomaly amplitude maximum of ±5 per cent (Figs 4c and d). However, to assess the resolution of the lower crustal velocity structure and, hence, the potential depth uncertainty of the Moho, and to assess the ability of this approach to discriminate between velocities of <7.0 km s^{-1} (normal lower oceanic crust) and >7.0 km s^{-1} and <7.3 km s^{-1} (undercrustal material), a defined structure recovery test was conducted in which two negative (−5 per cent) velocity anomalies were included in the starting model. Fig. 5 shows that small positive and negative anomalies are incorporated into the shallow subseabed region as the means of fitting the synthetic traveltime picks calculated from the starting model, and that a significant amount of vertical smearing of the anomalies actually recovered at depth also results. The conclusions to be drawn from this test are that the velocity uncertainty in the lower crust is higher at up to ±0.2 km s^{-1} and that if any undercrustal material is present, it is unresolvable with the seismic data alone unless >2 km in vertical and >25 km in lateral extent.

3.3 Results

Both the *FAST* and the *tomo2d* models confirm that the *rayinvr* model is largely a unique solution to the WA traveltime picks and that its interpreted features are clearly resolved by the observed data. The *rayinvr* model (Fig. 2) can be summarized as a succession of two discrete sedimentary packages overlying typical two-layered mature Atlantic oceanic basement with the upper mantle beneath

(Table 1). The most anomalous feature of the velocity–depth model is observed at the point where the F-STR intersects profile P01 (Fig. 1). In this region, high *P*-wave velocities are required in the shallowest subseabed layer, suggesting a structure that formed independently from standard oceanic basement accretion and subsequent sediment deposition. For a detailed description of the model interpretation itself, refer to Wilson *et al.* (2010) and Wilson (2011).

The overall aim of the WA seismic data modelling was to obtain the velocity structure and location of layer boundaries for input into 3-D 'whole plate' lithospheric flexure modelling. The *rayinvr* model was chosen as the ultimate, best-fitting, 2-D velocity–depth model (henceforth referred to as the *final* model) because it contains the necessary boundaries, defined in a simple layered model. The results of the modeller-independent inversions have confirmed that it is largely a unique solution and that it is also largely free from modeller bias. Systematic sensitivity testing of the forward model and checkerboard testing using the *FAST* and *tomo2d* inversion techniques, reveal that *P*-wave velocities may differ by ±0.1 km s^{-1} in the shallow subseabed layers, and by up to ±0.2 km s^{-1} in the lower basement layer and an acceptable fit is still achieved. On the same basis, the depth to the top of the oceanic basement is estimated to lie within ±0.1 km of the *rayinvr* model interface at worst, and the depth to the Moho is estimated to lie within ±0.5 km, increasing to ±1.0 km in areas of low P_mP and P_n phase coverage.

4 THREE-DIMENSIONAL FLEXURE

The rheology of the oceanic lithosphere is strongly temperature-dependent and as its age increases, it cools, thickens and becomes stronger. Effective elastic thickness (T_e) is used as a proxy for the long-term (>0.1 Ma) strength of a lithospheric plate and is approximately equivalent to the depth to the 450 °C oceanic isotherm based on the cooling plate model (e.g. Watts 2001). For Atlantic oceanic lithosphere, for example, T_e increases with age from ∼7–12 km at the mid-ocean ridge (Cochran 1979) to ∼40 km adjacent to the passive continental margin (Zheng & Arkani-Hamed 2002). The expected T_e can, thus, be predicted if the age of the plate is known. The flexural response of the lithosphere to external loading, such as by islands and seamounts, can also be analysed to reveal the apparent T_e. Any disagreement between the apparent and expected T_e implies that the strength of the plate has been altered by a process, independent of the normal mode of oceanic lithospheric evolution (Watts & Burov 2003).

In the region of the Cape Verde Islands, the lithosphere is 120–140 Ma, according to the correlation of magnetic lineations with the reversal timescale of the Earth's magnetic field (Müller *et al.* 2008), and the ages of the islands range from ∼20 to <3 Ma (Mitchell *et al.* 1983; Plesner *et al.* 2003; Duprat *et al.* 2007; Holm *et al.* 2008; Dyhr & Holm 2010; Madeira *et al.* 2010). At the time of loading, the ∼100–120-Myr-old lithosphere would be expected to have a corresponding T_e of 25–35 km, assuming a cooling plate model which has not subsequently been thermally reset (Parsons & Sclater 1977; Stein & Stein 1992).

By assuming that the geometry of marker horizons in the subsurface solely reflect the flexural response of the lithosphere to loading by the Cape Verde Islands [e.g. the angular unconformity between the Neogene flexural moat infill and the underlying pre-existing Mesozoic sediments observed throughout the region (Ali *et al.* 2003), and the sediment-top basement surface and the geometry of the Moho], it is possible to model this geometry and determine the apparent T_e, and, therefore, the apparent strength of the
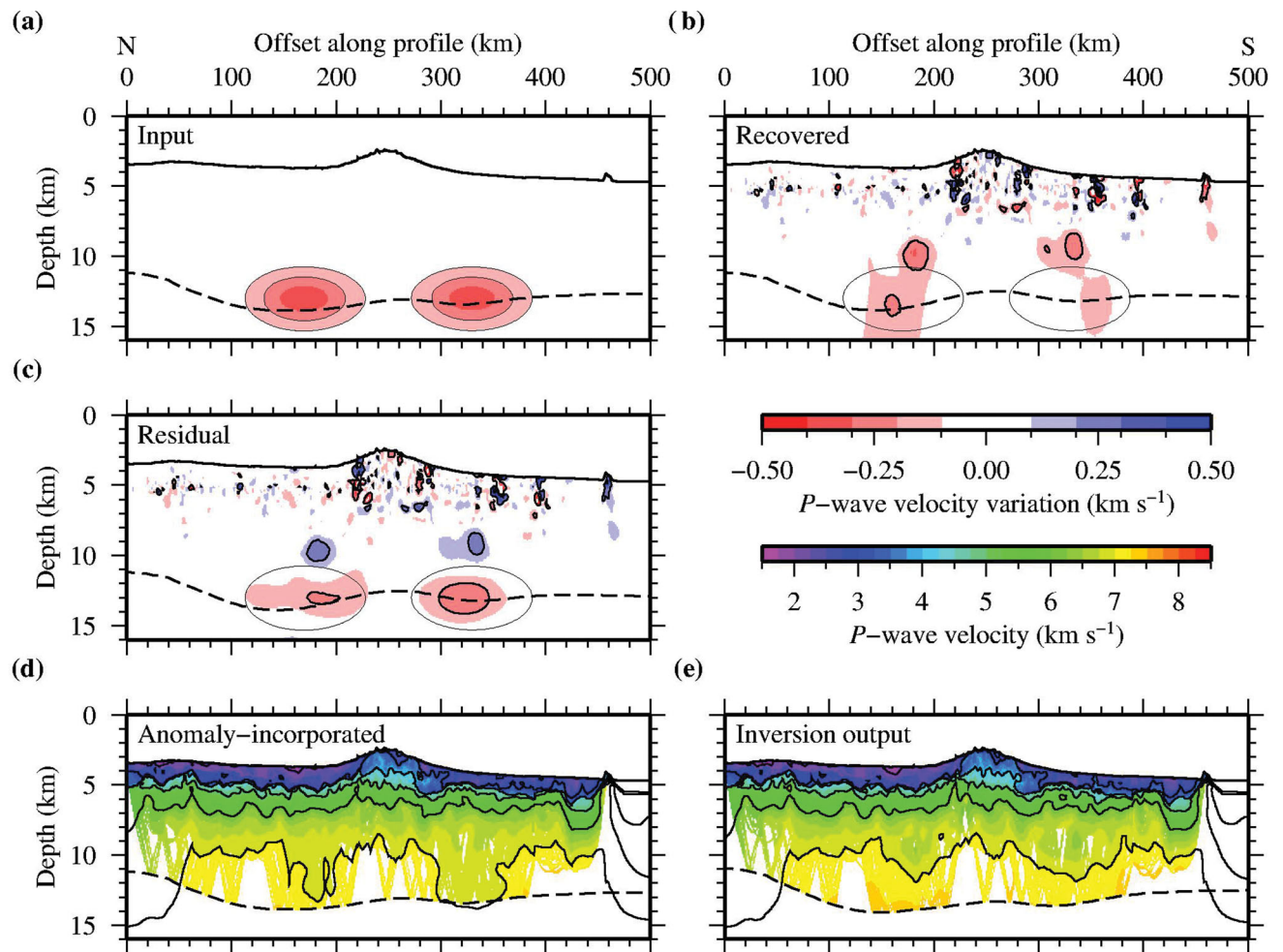
Figure 5. Resolution testing of the *tomo2d* model using two medium-sized negative anomalies (maximum amplitude -5 per cent) centred at 170 and 330 km profile offset. (a) Input anomaly pattern. (b) Anomaly recovered by the inversion. (c) Residual anomaly. (d) Anomaly-incorporated *tomo2d* model used to generate synthetic traveltime data. (e) Output model following an inversion of the new initial model using the checkerboard synthetic traveltime data. Black dashed lines mark the initial and final locations of the reflector. The black ovals in parts (a)–(c) highlight the input anomaly pattern and the anomalies are contoured at ± 0.2 km s^{-1}. Isovelocity contours are plotted in (d) and (e) with a 1 km s^{-1} contour interval. Parts (d) and (e) are masked according to ray coverage.

Table 1. Layering structure of the *rayinvr* model.

Model layer	Thickness (km)	Upper velocity (km s^{-1})	Lower velocity (km s^{-1})	Velocity gradient (s^{-1})
Water column	~4.0	1.49	1.51†	0.005
Shallow subseabed 1	0.3–1.0	1.90–3.00	2.20–3.40	~0.50
Shallow subseabed 2	0.5–1.0 (2.0)	2.50–3.60	2.70–4.30	~0.75 (0.50)
Upper oceanic basement	1.0–2.0	4.30–4.80	4.90–6.10	~0.63
Lower oceanic basement	4.0–7.0	6.40–6.70	7.10–7.30	~0.11
Upper mantle	–	7.70	–	~0.03

†The lower velocity of the water column quoted here has been calculated using the velocity gradient and the average seabed depth of 4 km b.s.l. Values in brackets for shallow subseabed layer 2 are taken from 250 km profile offset, and are representative of the high-velocity region beneath F-STR.

lithospheric plate on which the islands were emplaced. The first step is, therefore, to determine the surfaces of flexure and the volume and extent of the load. The *final* 2-D velocity–depth model delineates the shapes of the intrasediment unconformity, the basement and Moho interfaces, with the geometry and depth of the intrasediment horizons corroborated by a depth conversion of the MCS data using the WA model velocities. There are two aspects to estimating the load: first, determining the volume of the islands and, secondly,

determining the volume and extent of regional sediment deposition and the localized sediment infill of the flexural moat around each island.

Ali *et al.* (2003) mapped the two-way traveltime (TWTT) 'thickness' of the Neogene moat infill unit, which comprises a mixture of pelagic and volcaniclastic sediments, along all available seismic reflection profiles in the region. In this study, to determine the volume of the sediment load, a surface was fit to these data to reveal

the approximate amplitude and wavelength of the basin into which the sediments were deposited. This TWTT 'thickness' was then converted to actual thickness using the average *P*-wave velocity of the shallowest layer in the *final* 2-D velocity–depth model from the region to the north of the F-STR, 2.1 km s^{-1}. This velocity is, however, lower than that determined for moat sediments surrounding other islands including the Canaries and Hawaii, where moat infill velocities of 2–5 km s^{-1} (Watts *et al.* 1997) and >3.7 km s^{-1} (Rees *et al.* 1993) have been reported.

In contrast, Ali *et al.* (2003) determined the *P*-wave velocity of the moat infill unit to range from 2.5 to 3.2 km s^{-1}. These velocities were obtained primarily from MCS stacking velocities, which were tied to downhole velocity measurements made only at a single DSDP borehole (site 368). Ali *et al.*'s (2003) higher velocities result in a greater thickness of the moat infill sediments than the *final* 2-D velocity–depth model predicts. Despite the unusually low velocity reported here, the thickness of the sediments determined in this study is considered a more reliable estimate because the interval velocity used to convert the TWTT sediment thickness map to depth not only is independently determined from the WA data, but it is also determined along the majority of swell transect profile P01 (Fig. 1).

The thickness of the moat infill sediments generally increases towards the islands (Fig. 6a). The main depositional basin is approximately circular, centred halfway between the eastern islands of Maio and Boa Vista where the sediment thickness reaches a maximum of ∼1.2 km. A secondary area of thicker deposition extends to the northwest and correlates with the location of São Nicolau, São Vicente and Santo Antão. Although the island of Fogo reaches the highest elevation in the archipelago, the infill sediments do not show a strong pattern of thickening around it. The lack of a strong flexural signature around Fogo and Brava may be due to a combination of the limited lateral extent of the submarine edifice and their young age compared to the other islands—Fogo has erupted in the historical past while <3 Ma eruption ages are obtained for Brava (Madeira *et al.* 2010).

To determine the volume and spatial extent of the island load, a directional median filter (Kim & Wessel 2008) of width 240 km was used to define the long-wavelength regional bathymetric gradient (i.e. the swell), which was subtracted from the bathymetry. The load is predominantly composed of medium-to-high-density igneous material that was magmatically emplaced onto the crust during island building.

A density model was constructed from the *final* velocity–depth model by converting the isovelocity layer interval velocities into density using a two-part velocity–density curve, derived from the relationship of Hamilton (1978) for velocities ≤3.7 km s^{-1} and Carlson & Raskin's (1984) relationship for oceanic crustal rocks for velocities >3.7 km s^{-1}. The density of the igneous part of the oceanic crust ranges from 2500 to 3000 kg m^{-3}, with an average value of 2850 kg m^{-3}, and the core component of the load is expected to have a similar density. During island growth, particularly in a subaerial environment, erosion processes rework material derived from the volcanic edifices, depositing it downslope. Such erosion and mass wasting deposits also contribute to the total load driving the flexure, although this material would have a lower bulk density as porosity increases during reworking. Overall, the load is expected to have an intermediate density of ∼2700 kg m^{-3}.

In the final step, we have used a spectral technique based on the Fast Fourier Transform (FFT) to compute the 3-D flexure (e.g. Walcott 1976) due to the driving load. We use a model of a uniform elastic thickness plate with the density of the volcano load equal to the density of the material that infills the flexure. Such an approach does not distinguish between the high-density material expected to comprise the volcano load that is emplaced on the surface of the crust and the lower density sediments derived from mass wasting of the volcano that infills the flexure. For each choice of T_e used iteratively during modelling, we calculated the infill density (ρ_{infill}) using the fraction (by volume) of infill material beneath the driving load (F_{load}) to control the relative contribution from the load and sediment densities (ρ_{load} and ρ_{seds}) according to the following equation:

$$\rho_{infill} = \rho_{seds} + F_{load}(\rho_{load} - \rho_{seds}). \tag{1}$$

The flexure was calculated for a range of different load densities (every 100 kg m^{-3}, from 2200 to 2900 kg m^{-3}) and plate strengths defined by the T_e parameter (every 10 km, from 0 to 70 km) with limits chosen to reflect the maximum range expected for oceanic lithosphere. The calculated flexure was then compared to the observed thickness of moat infill sediments and the rms misfit was assessed to determine the best-fitting load density and T_e parameter pair.

The rms misfit between modelled flexure and observed moat infill thickness (Fig. 6b) shows a correlation between increasing load density and increasing T_e, and reaches a minimum at a T_e of 60 km and a load density of 2600 kg m^{-3}, corresponding to an infill density of 2144 kg m^{-3}. As the best-fitting load density of 2600 kg m^{-3} is only slightly lower than expected (2700 kg m^{-3}), the preferred model, chosen to match the observed flexure within the broad minimum zone of rms misfit, is for a load density of 2700 kg m^{-3}. This represents basaltic ocean island material, coupled with a T_e of 60 km.

5 THREE-DIMENSIONAL GRAVITY ANOMALY

As an independent test of the preferred (T_e of 60 km) flexure model, the crustal component of the free-air gravity anomaly (FAA) was calculated using a 3-D FFT method (e.g. Parker 1972) with $n = 4$, where *n* is the number of iterations in the series expansion for the gravity effect of each surface of flexure. Density contrasts across each flexure surface were derived from the *final* WA seismic model and the total contribution of the flexure of the top and base of the crust calculated and compared to the observed FAA.

To consider the surface loading related solely to the islands, it is first necessary to remove the long-wavelength component of the observed FAA, which represents the bathymetric swell and its regional compensation. The spherical harmonic representation of the observed satellite gravity field (OSU91A—Pavlis & Rapp 1990), complete to degree and order 40 (Fig. 7a) was chosen to represent deep-seated gravity anomalies with wavelengths >1000 km that are unrelated to surface load-induced plate flexure and, instead, are associated with the regional topographic swell and its compensation. Ali *et al.* (2003) use a spherical harmonic $n = m = 40$ for the gravity anomaly and a median filter with w = 500 km for the bathymetry because they found that this best described the observed gravity anomaly and bathymetry associated with the Cape Verdes Swell. Subsequently, Kim & Wessel (2008) concluded that such a median filter would oversmooth the swell topography and, instead, a directional median filter should be used. To isolate the long-wavelength anomalies we have, therefore, followed Ali *et al.* (2003) for the gravity and Kim & Wessel (2008) for the bathymetry. The resulting gravity 'swell anomaly' has been removed from the observed FAA
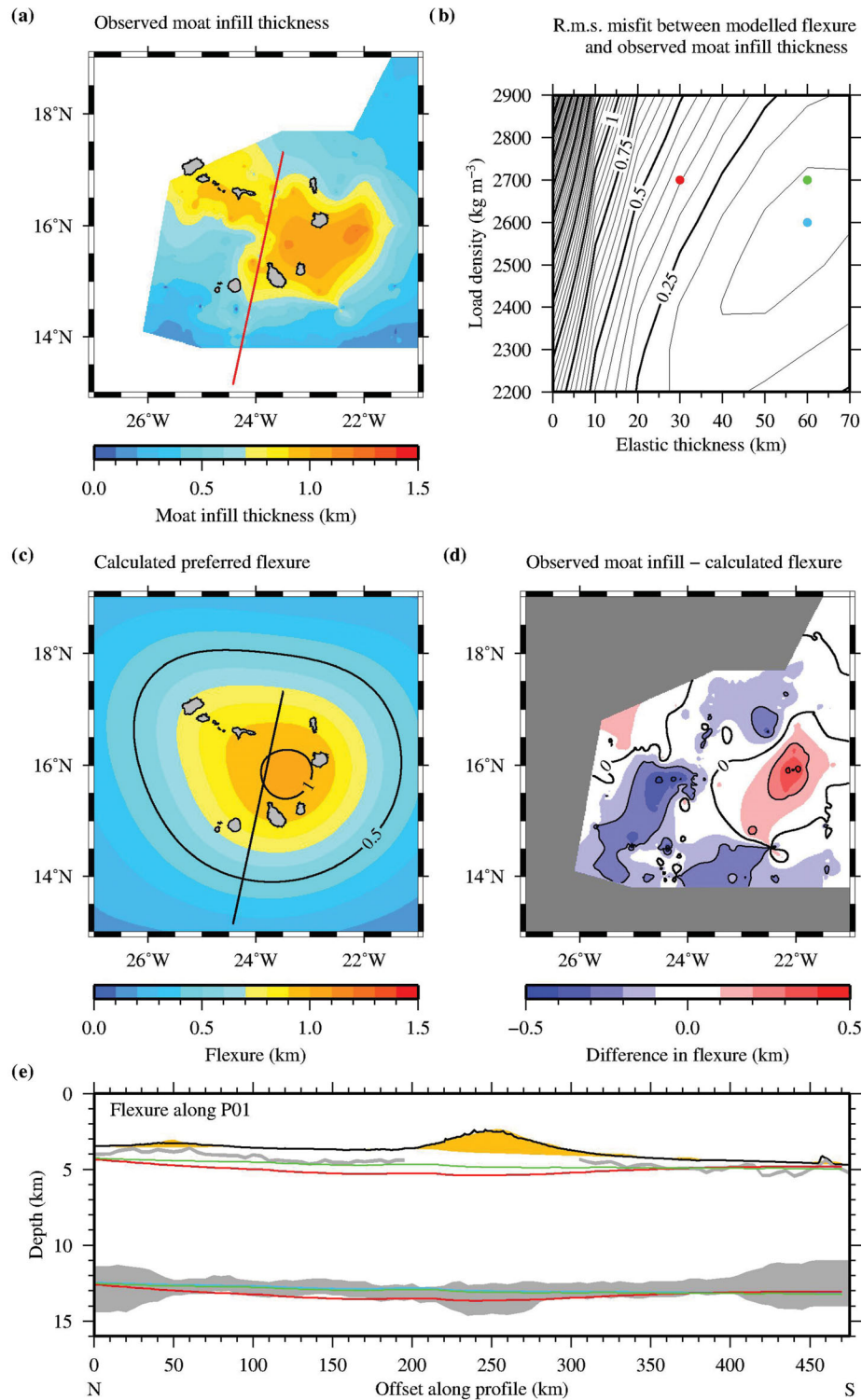
Figure 6. Summary of flexure calculated using an intermediate density (scaled according to load density and T_e—Wilson 2011) for the infill material. (a) Moat infill sediment thickness, converted from the TWTT isochron surface using an interval velocity of 2.1 km s^{-1} obtained from the *final* 2-D velocity–depth model. Thickness contours (black lines) have a 0.5 km contour interval. (b) rms misfit between observed moat infill sediment thickness and calculated flexure within the range of tested load densities and values of T_e. Misfit contours (black lines) with a 0.05 km interval. Best-fit, expected and preferred parameter pairs are indicated (blue, red and green dots, respectively). (c) Regional flexure calculated for the preferred parameter pair. Flexure contours (black lines) with a 0.5 km contour interval. The location of profile P01 (black line) is also shown. (d) Difference between observed moat infill sediment thickness and the preferred calculated flexure masked with areas of observed data. Positive values indicate areas where the calculated flexure underestimates the observed thickness. Difference contours (black lines) with a 0.2 km contour interval. (e) Comparison of the flexure calculated crust with the seismically determined layer boundaries along profile P01. The seabed (black line), unconformity and Moho (grey bands including uncertainty) from the *final* 2-D velocity–depth model are compared to the driving load (orange shading) and the top and base of the crustal model resulting from the flexure calculation for the best-fit, expected (based on plate age) and preferred parameter pairs (blue, red and green lines respectively). See text for discussion.
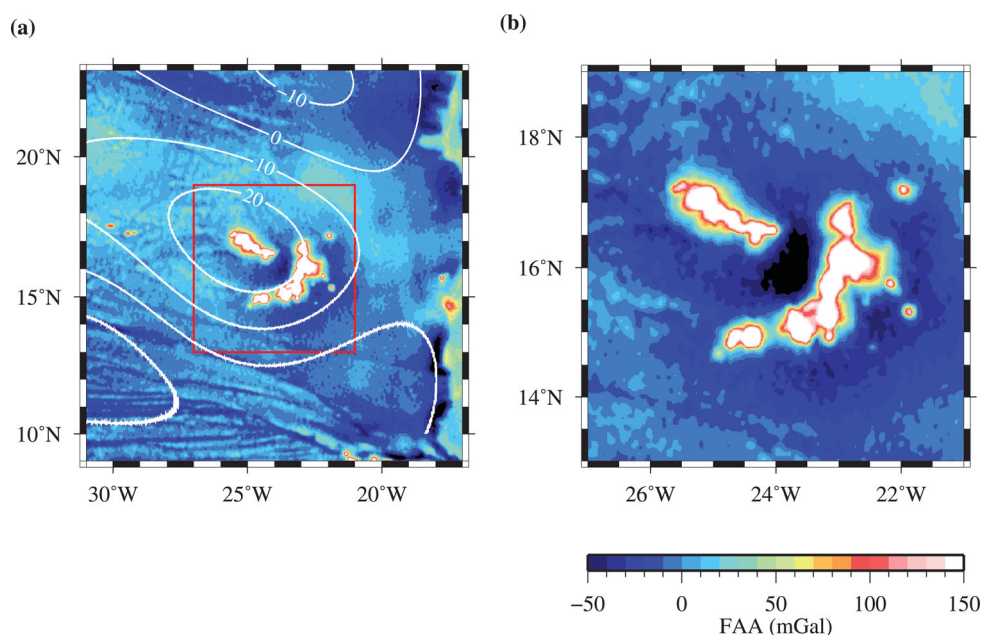
(a)   (b)

Figure 7. Long-wavelength component of the FAA. (a) Comparison of the OSU91A (Pavlis & Rapp 1990) satellite-derived gravity anomaly complete to degree and order $n = m = 40$ including anomalies with wavelengths >1000 km (white contours with a 10-mGal contour interval), with the observed FAA. The area used for comparison with results from a 3-D FFT calculation is also shown (red box). (b) The observed FAA with the long-wavelength component in (a) removed is used to assess the fit of the gravity anomalies calculated from the flexure models. The short-wavelength positive anomalies of the islands are superimposed on a medium-wavelength negative anomaly that is approximately centred beneath the load.

to produce the crustal gravity anomaly (Fig. 7b), against which the calculated anomaly can be compared.

The calculated gravity anomaly for the preferred flexure model (Fig. 8a) is similar to the observed (Fig. 7b) and a plot of the residual anomaly (Fig. 8b) shows that the observed crustal gravity anomaly is generally matched to ±30 mGal. Around the eastern islands, where the highest amplitude flexure occurs (see Fig. 6c), the resulting gravity low is undercalculated by up to ∼40 mGal, suggesting that the modelled plate is too rigid and does not flex sufficiently to accommodate a large enough volume of low-density infill material to reproduce the observed negative gravity anomaly.

Over the islands and their edifices, the gravity anomaly calculated from the flexure model is considerably less than the observed, in some cases by >50 mGal. Increasing the density of the infill material directly beneath the load, where it is underestimated due to the limitation of the model parametrization, would only account for <10 mGal of the mismatch. However, the satellite-observed gravity data have a much lower spatial resolution over land and regions of shallow bathymetry, particularly for short-wavelength features, such as ocean islands and seamounts (Sandwell & Smith 1997; Marks & Smith 2007; Sandwell & Smith 2009). It is evident that the 0.5 km bathymetric contour outlines the large amplitude highs in the residual anomaly (Fig. 8b). Excluding the areas within the 0.5 km bathymetric contour, the overall rms misfit between the calculated gravity anomaly for the preferred flexure model and the observed is reduced to 10.9 mGal.

In comparison, the calculated gravity anomaly for the flexure model with a T_e of 30 km, expected based on plate age at the time of loading (Fig. 8c), shows a closer match to the observed crustal gravity anomaly (Fig. 8d). Again, if the areas within the 0.5 km bathymetric contour are excluded, the rms misfit is only 10.1 mGal. This model clearly explains the observed gravity anomaly but as demonstrated in Fig. 6(e), the calculated amplitude of flexure for

this model is too high and does not match the observed moat infill sediment thickness/geometry of the sediment-basement interface.

Assuming a constant T_e, therefore, leads to a contradiction:

(1) T_e of 30 km—flexural modelling predicts a plate surface that is more flexed than observed while calculation of the expected gravity anomaly modelling produces a good fit based on the volume and density of the island and infill loads derived from seismic observations, whereas

(2) T_e of 60 km—flexural modelling produces a good fit between observed and calculated flexural surface markers (intrasediment, sediment-basement and Moho) while calculation of the expected gravity anomaly modelling produces a significant misfit.

6 ELASTIC THICKNESS OF THE LITHOSPHERE

It is not possible, by conductive cooling alone, for the inherent strength of the plate to have a higher value than predicted, as the lithosphere does not cool and thicken above a certain rate (e.g. Stein & Stein 1992). Instead, the high strength can only be an apparent one. The Cape Verde region exhibits good evidence to support uplift (e.g. Lancelot *et al.* 1978a,b; Stillman *et al.* 1982), with Jurassic sediments on the islands, a flexural moat sequence that is tilted upwards away from the islands rather than downwards towards the islands (as it is, e.g. at the Hawaiian and Canary islands) and, of course, a well-developed topographic swell.

If it is assumed that the T_e of the lithosphere was 30 km at the time of loading as the gravity anomaly suggests, a subcrustal, upward-acting load could instead counteract the corresponding excess flexure. Ali *et al.* (2003) developed such a model and concluded that the observed moat infill thickness could be matched using a constant load and infill density of 2700 kg m^{-3} if an upward-acting load with 20 per cent of the mass of the surface load is also included.
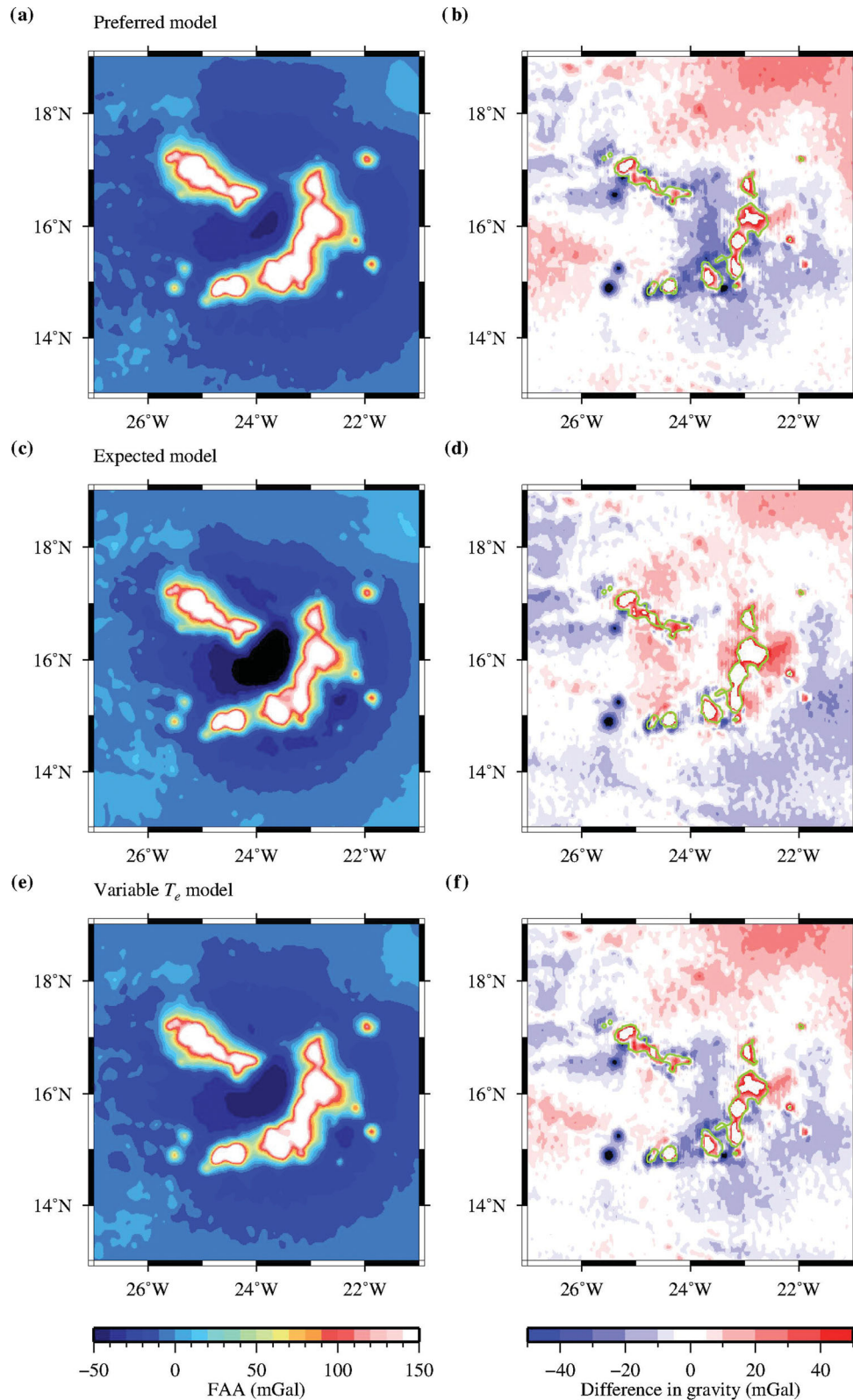
Figure 8. Summary of gravity anomalies calculated using an intermediate density (scaled according to load density and T_e—Wilson 2011) for the infill material for the preferred model (a), the expected model (c), and the variable T_e model (e). Difference between the observed FAA with the long-wavelength swell component removed (Fig. 7b) and the preferred, expected and variable T_e models are shown in (b), (d) and (f), respectively. The 0.5 km bathymetry contour (green line) encloses the islands and their steep submarine flanks where the observed FAA is inaccurate and, hence, omitted from the statistical analysis. See text for discussion.

For synchronous surface and undercrustal load emplacement, whereby the undercrustal load has the same spatial distribution as the surface load, the magnitude of uplift relative to downward flexure is directly proportional to the mass of the undercrustal load as a fraction of the surface load. A range of subcrustal load fractions, from 0 to 1 (0–100 per cent), were tested by comparing the total deflection (the sum of downward flexure and uplift) to the observed moat infill thickness and determining the rms misfit. The best-fitting total deflection was obtained for a load fraction of 0.3 (30 per cent) and the results are summarized in Fig. 9.

With this model the difference between the total deflection and the observed moat infill thickness (Fig. 9d) is generally <0.5 km and predominantly <0.2 km. However, there is a larger area where the calculated flexure is too low, and that shows a direct relationship with increasing distance from the driving load, implying that a long-wavelength component of flexure is missing from the solution.

The required volume of the undercrustal load can be determined from the best-fitting mass fraction, a similarly determined density ratio and the modelled volume of the load that is driving surface flexure. Using a density of 3000 kg m^{-3} for the undercrustal load, which is representative of the high-density igneous material that may be accumulated at the base of the crust during island building magmatism, this gives rise to a negative density contrast of -300 kg m^{-3} with the surrounding mantle material. The majority of the driving load is submarine and has a positive density contrast with the water column of 1700 kg m^{-3}, resulting in a density ratio of ~0.2. By conservation of mass, for an undercrustal load to provide uplift to counteract the flexure sufficiently to match the geometry of the observed sediment-basement surface, it must have a volume that is at least 1.5 times that of the surface load. Fig. 9(e) shows a comparison of the basal surface of such a load to the seismically determined Moho along profile P01, and demonstrates that this amount of undercrustal material, if present, would exceed the maximum uncertainty in Moho depth derived from the WA seismic subsurface imaging.

The predicted depth of the basal load surface is also compared to the Moho depth estimates of Lodge & Helffrich (2006) in Table 2, at the locations of land-based recording stations located on seven of the islands. As with the Moho along profile P01, there is also a significant discrepancy (>2 km) between the depths calculated from analysis of receiver functions (Lodge & Helffrich 2006) and those required by the model. The northwest chain of islands together with Fogo, require a larger undercrustal load in the flexure model than the 1-D structural models derived from receiver function analyses suggest, while the islands of Sal and Maio require less. Santiago is the only island beneath which the two estimates are in effective agreement, with a difference of just 0.6 km. While the WA seismic data do not preclude the occurrence of undercrustal material beneath the islands, the flexure modelling implies that, if it does exist, it cannot be of a large enough volume to sufficiently counteract the surface loading such that it matches the observed geometry of the sediment-basement surface (i.e. the moat infill thickness), if the lithosphere has a constant T_e of 30 km. However, since we do not know the true spatial extent of the apparent upward-acting load, the results and implications of the approach we have adopted should be regarded as an approximation only.

7 VARYING T_e

This study has shown that models that are parametrized with a single, constant value of T_e do not result in a pattern of flexure

that adequately matches both the observed moat infill thickness or geometry of the sediment-basement surface and Moho at all wavelengths. Instead, models with a high and age-related apparent T_e can explain different characteristics of the flexure to a large extent. This apparent contradiction may be explained if there are two effective components to the loading where during the first stage of loading, which might represent early island growth, the lithosphere has an inherent T_e of 30 km (i.e. that predicted for its age), and during the second stage an upward-acting load unbends the plate, making it appear stronger than it actually is—that is overall expressing flexural characteristics of a T_e of 60 km. To test this multicomponent hypothesis, the flexural response was calculated by combining a fraction of the total flexure that occurs for the expected T_e of 30 km (Fig. 10a) with the remaining fraction of flexure that occurs for the best-fitting T_e of 60 km (Fig. 10b) to simulate a change in T_e.

To consider the possibility of a varying T_e, a multicomponent model was created by summing 30 per cent of the total flexure associated with a T_e of 30 km and 70 per cent of the total flexure associated with a T_e of 60 km (Fig. 10c), as this ratio produced the statistical best-fit to the observed moat infill sediment thickness/sediment-basement surface geometry proximal to the islands. However, comparing the difference between the calculated flexure and the observed moat infill thickness (Fig. 10d) for the multicomponent model, to that of the preferred constant T_e model (Fig. 6d), shows that this result overestimates the flexure by >0.2 km at the regional scale. Therefore, it is likely that T_e also varies spatially, whereby the strength of the lithosphere may also be affected on the local scale by thermal rejuvenation of the lithosphere directly associated with the island building process.

Temporal variation in T_e could also occur by load-induced stress relaxation by thermally activated creep (diffusion or dislocation), which would progressively reduce the thickness and, hence strength, of the lithosphere that supports the load from its short-term (seismic) thickness to its long-term (elastic) thickness (Watts & Zhong 2000). A high T_e in this case would imply that a significant proportion of the edifice of the Cape Verde Islands is young (<1–2 Myr) and so has not yet fully relaxed, although current surface geological observations appear to contradict such a young age for the majority of the islands (Holm *et al.* 2008 and references therein).

An estimate of the gravity anomaly produced by the multicomponent T_e model was also determined by summing the equivalent fractions of the end-member anomalies (Fig. 8e). The rms misfit between the calculated and observed crustal gravity anomalies is 9.8 mGal (Fig. 8f). Compared to the result from the preferred flexure model (Fig. 8b), the gravity mismatch is reduced where the highest amplitude of flexure occurs, but fits equally well over the rest of the region. In areas distal to the load, the gravity mismatch is comparable to that observed for the model with a T_e of 30 km (Fig. 8d).

This multicomponent T_e model is, hence, regarded as the 'best-fitting' model, considering the fit to both the observed moat infill thickness, sediment-basement surface geometry and the crustal gravity anomaly. However, a negative anomaly of amplitude -40 mGal and wavelength ~350 km, located at the eastern islands, is still unaccounted for.

8 CAPE VERDE SWELL

Results of the 3-D flexure and gravity modelling suggest that, during surface loading or some time subsequently, an upward-acting force has counteracted some of the surface load-induced subsidence,
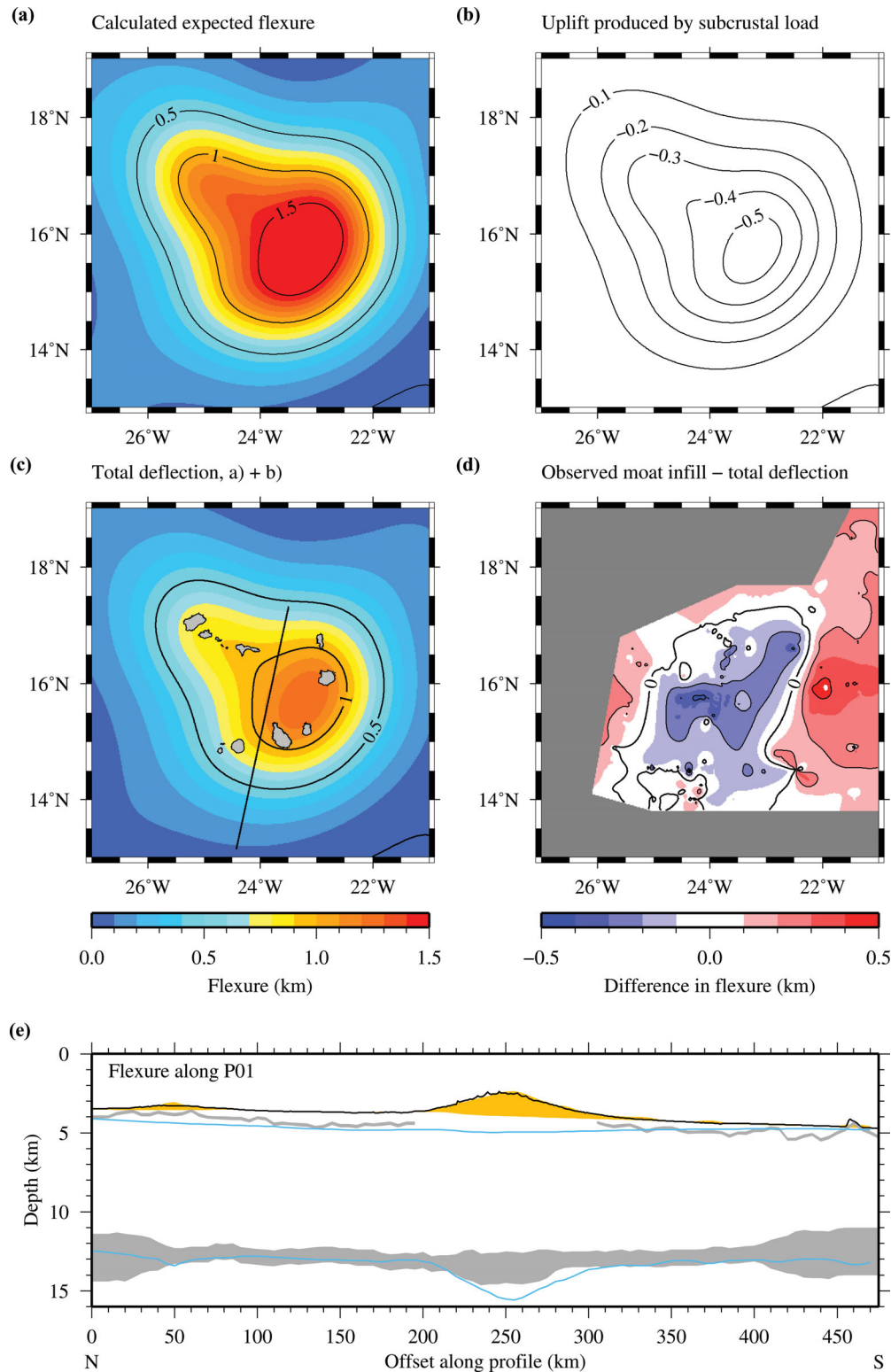
Figure 9. Flexure calculated from a model incorporating an upward-acting load at the base of the crust, assuming the expected value of T_e of 30 km. (a) Regional flexure calculated using the intermediate density (2245 kg m^{-3}) infill material and load density of 2700 kg m^{-3}. Flexure contours (black lines) with a 0.5 km contour interval. (b) Uplift (negative flexure) expected for an undercrustal load, with a subcrustal load fraction of 0.3. Uplift contours (black lines) with a 0.1 km contour interval. (c) Total deflection (sum of flexure and uplift) for the best-fitting subcrustal load fraction of 0.3. Flexure contours (black lines) with a 0.5 km contour interval. Location of profile P01 (black line) is also shown. (d) Difference between observed moat infill sediment thickness and the best-fitting total deflection masked with areas of observed data. Positive values indicate areas where the calculated flexure underestimates the observed thickness. Difference contours (black lines) with a 0.2 km contour interval. (e) The seabed (black line), unconformity and Moho (grey bands including uncertainty) from the *final* 2-D velocity–depth model are compared to the driving load (orange shading) and the top and base of the crustal model resulting from the flexure calculation for the best-fitting parameter pair (blue lines). Note that the calculated base of crust includes the undercrustal load. See text for discussion.

Table 2. Comparison of the depth to the Moho beneath the Cape Verde Islands determined using receiver function analysis (Lodge & Helffrich 2006) with those calculated during flexure modelling with an undercrustal load.

Island	Station latitude (N)	Station longitude (W)	Moho depth from receiver functions (km)	Moho depth undercrustal load (km)
Santo Antão	16°59′	25°12′	~10	18.9
São Vicente	16°52′	24°56′	~15	18.7
São Nicolau	16°37′	24°21′	~10	19.5
Sal	16°44′	22°56′	~20	17.7
Maio	15°14′	23°11′	~23	18.8
Santiago	14°58′	23°36′	~19	19.6
Fogo	14° 55′	24° 23′	~13	22.5

making the lithosphere appear stronger than expected based solely on its age. The volume of undercrustal material, required to produce sufficient uplift to reduce the calculated flexure produced by surface loads given a T_e of 30 km, exceeds the uncertainties of the *final* 2-D velocity–depth model (Fig. 9e) and other estimates of crustal thickness throughout the region (Table 2). These results imply that the mechanism causing uplift originates at a much greater depth, deeper than is resolvable using WA seismic methods, either within the lower lithosphere, in the asthenosphere, at the lithosphere–asthenosphere boundary, or some combination of these.

The long-wavelength topography of the swell, defined by applying a directional median filter (Kim & Wessel 2008) of width 240 km to the observed bathymetry (GEBCO—IOC, IHO & BODC 2003), can be related to long-wavelength gravity and geoid anomalies that result from density variations in the lithosphere and asthenosphere. If the region is assumed to be in isostatic equilibrium, analysis of the gravity–topography slope (e.g. Watts 1976) or the geoid–topography ratio (e.g. Cazenave *et al.* 1988) can provide insight into the depth of the density variation.

The long-wavelength gravity anomaly is the sum of two components: a positive anomaly resulting from the elevated swell topography and a negative anomaly due to the causative low-density region. If the causative region is closer to the reference datum (sea level), a low gravity–topography slope would be expected. In contrast, if the low-density region is at a greater depth, the positive anomaly from the swell topography should be dominant, resulting in a high gravity–topography slope. Using the gravity–topography slope (gravitational admittance), $Z(k)$, it is also possible to calculate the expected compensation depth (D_c) of the swell using the following formula (e.g. Watts 2001):

$$D_c = \frac{Z(k)}{2\pi G(\rho_m - \rho_w)k},\qquad(2)$$

where G is the gravitational constant, k is the wave number ($2\pi/\lambda$), λ is the characteristic swell wavelength of 2000 km and ρ_m and ρ_w are the densities of the mantle (3330 kg m^{-3}) and the water column (1030 kg m^{-3}), respectively.

Similarly, long-wavelength positive deflections of the geoid are reduced if the compensation is close to the Earth's surface. Sandwell & MacKenzie (1989) summarized that low geoid–topography ratios (0–2 m km^{-1}) are indicative of shallow Airy compensation, intermediate ratios (2–6 m km^{-1}) provide evidence of average compensation depths of between 50 and 80 km, whereas high ratios (>6 m km^{-1}) represent dynamic support by convective stress at the lithosphere–asthenosphere boundary. A global analysis of the geoid–topography ratio at oceanic plateaus and swells (Marks & Sandwell 1991) reveals a maximum of just 4.7 m km^{-1}, apparently excluding the possibility of a dynamic support mechanism. Using the geoid–topography ratio ($\Delta N/\Delta h$) it is possible to obtain a more

precise estimate of the compensation depth using the following formula, based on Pratt isostasy (Haxby & Turcotte 1978):

$$\frac{\Delta N}{\Delta h} = \frac{\pi G}{g}(\rho_m - \rho_w)D_c,\qquad(3)$$

where G is the gravitational constant and g is the mean surface gravity.

The bathymetry of the swell was converted into anomalous topography (Fig. 11a) above the expected bathymetry for the age of the lithosphere based on the GDH1 model of cooling and subsidence (Stein & Stein 1992). The residual gravity anomaly (Fig. 7b) is further reduced by removing the spherical harmonic component of the satellite gravity field complete to degree 10, which includes gravity anomalies with characteristic wavelengths >4000 km that arise from deep-seated density variations in the asthenospheric mantle (Bowin 1983; Fig. 11b). Similarly, the long-wavelength positive geoid anomaly associated with the swell (Fig. 11c), complete to spherical harmonic degree and order $10 < n = m < 40$, was extracted from the EGM96 model (Lemoine *et al.* 1998) to reflect the signature of the swell and its compensation (wavelengths between 1000 and 4000 km).

Estimates of the gravity–topography slope or geoid–topography ratio were obtained using linear regression on the spatial averages of these data (e.g. Watts 1976; Sandwell & MacKenzie 1989). The spatial averages of swell topography, gravity and geoid anomalies were calculated for $1° \times 1°$ bins over the area shown in Fig. 11. Plots of both gravity and geoid anomalies against topography for these averages reveal a large degree of scatter and there is no clear correlation between the pairs of variables. Consequently, an alternative method was employed, similar to that used by Monnereau & Cazenave (1990), which involved the analysis of the gravity–topography slope and geoid–topography ratio along radial profiles extending from the swell crest at 17°00′N 23°30′W. Profiles were generated at an angular increment of 20°. Profiles heading east were excluded due to the influence of the adjacent African continental margin on the topographic anomaly. Data were extracted from the grids every 20 km along these profiles and the results are plotted in Figs 11(d) and (e).

Although there is some variability in the gravity–topography and geoid–topography gradients, both along individual and between all the profiles, the results show averages (using only data from profiles with clear linear relationships—blue lines in Fig. 11) for the gravity–topography slope and geoid–topography ratio of 16.6 ± 1.9 mGal km^{-1} and 3.77 ± 0.38 m km^{-1}, respectively, that match the overall trend particularly where the topographic anomaly is <1 km. The calculated gravity–topography slope is slightly lower than the estimate of Crosby *et al.* (2006) who reported a slope of between 20 and 27 mGal km^{-1} and the average geoid–topography ratio is also lower than the value of 4.4 m km^{-1} obtained by Grevemeyer (1999).
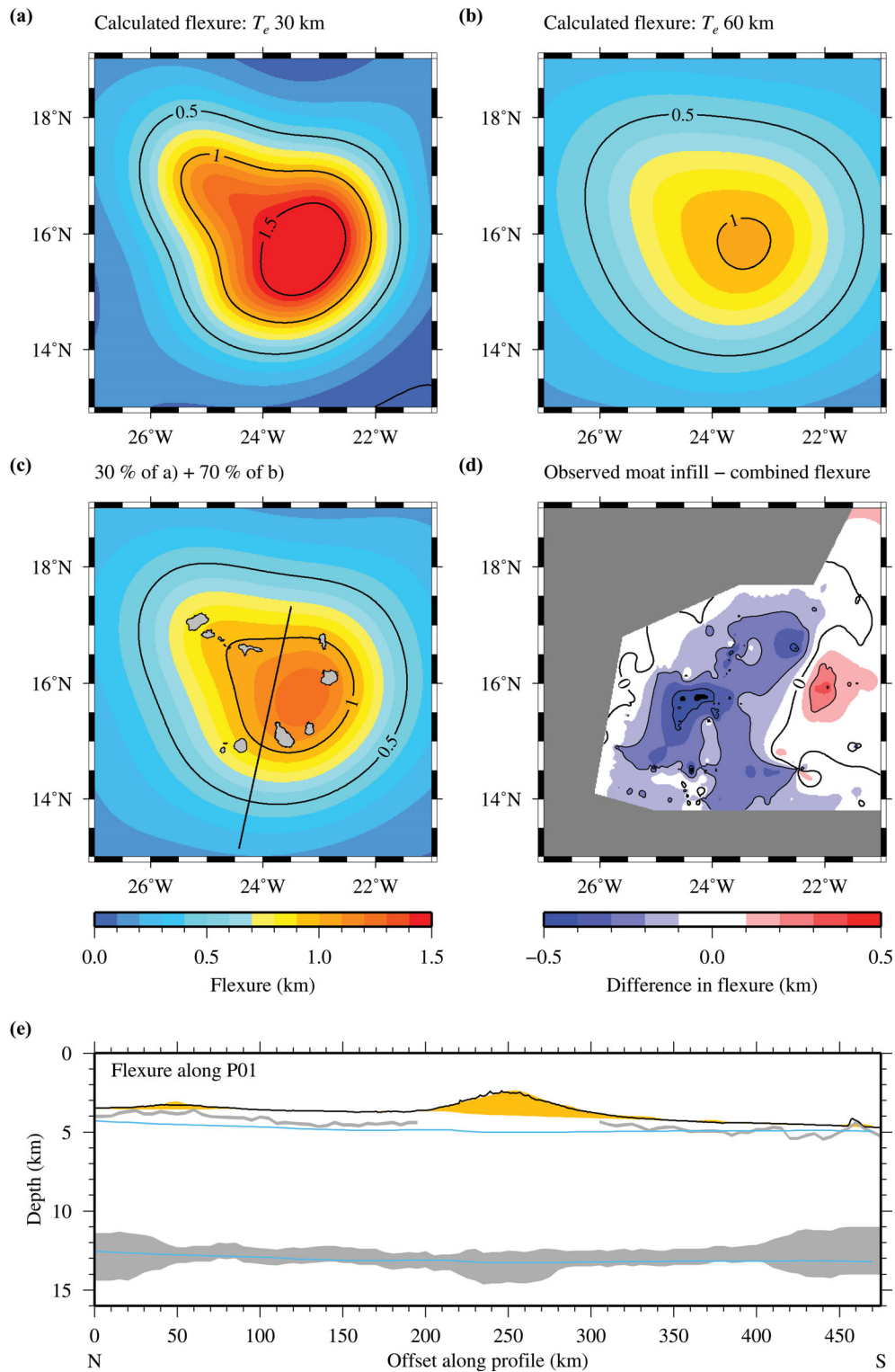
Figure 10. An estimate of the flexure associated with a variable T_e. (a) Regional flexure calculated using the intermediate density (2245 kg m^{-3}) infill material, load density of 2700 kg m^{-3} and a T_e of 30 km. Flexure contours (black lines) with a 0.5 km contour interval. (b) Regional flexure calculated using the intermediate density (2170 kg m^{-3}) infill material, load density of 2700 kg m^{-3} and a T_e of 60 km. Flexure contours (black lines) with a 0.5 km contour interval. (c) Expected flexure for a combined model with variable T_e (30 per cent at 30 km, 70 per cent at 60 km). Flexure contours (black lines) with a 0.5 km contour interval. Location of profile P01 (black line) is also shown. (d) Difference between observed moat infill sediment thickness and the calculated flexure for the variable T_e model, masked with areas of observed data. Positive values indicate areas where the calculated flexure underestimates the observed thickness. Difference contours (black lines) with a 0.2 km contour interval. (e) Comparison of the flexure calculated crust with the seismically determined layer boundaries along profile P01. The seabed (black line), unconformity and Moho (grey bands including uncertainty) from the *final* 2-D velocity–depth model are compared to the driving load (orange shading) and the top and base of the 1-D model of the crust resulting from the flexure calculation for the variable T_e model (blue lines).
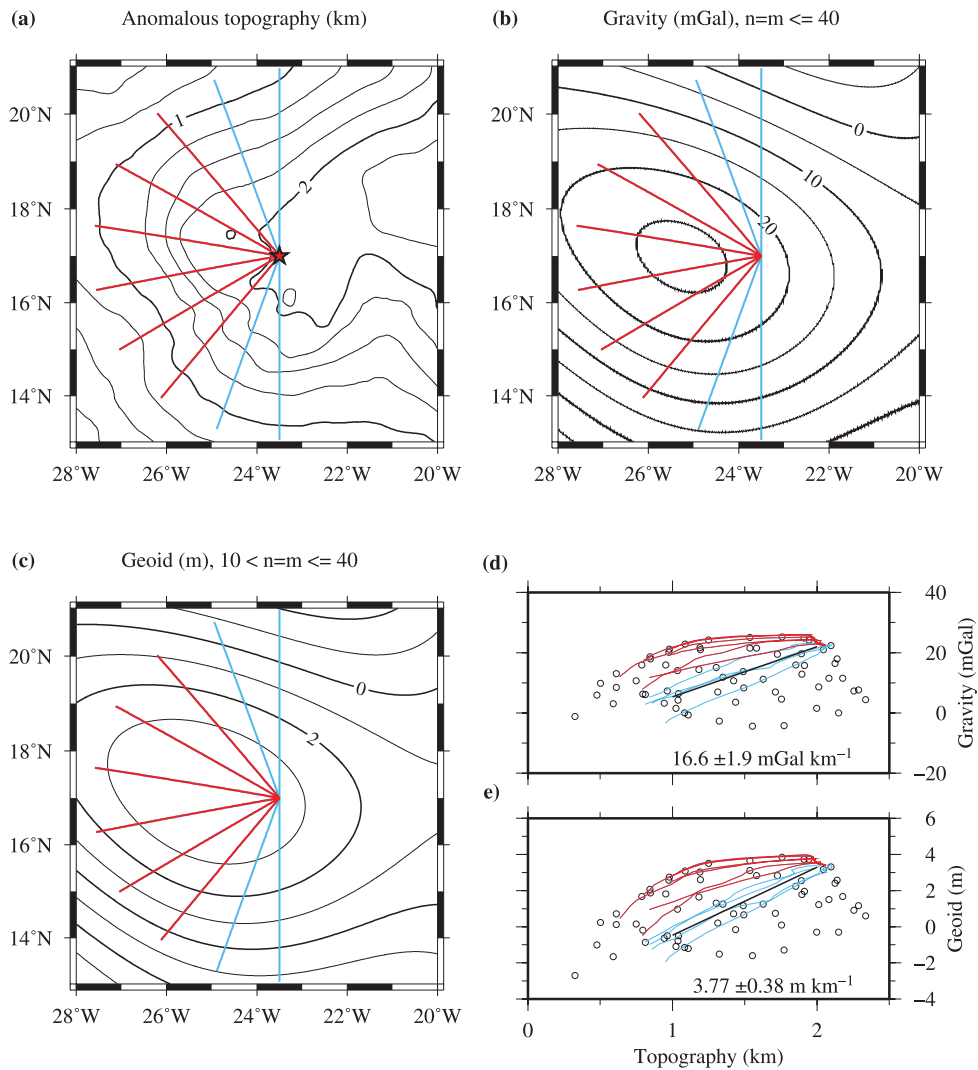
Figure 11. Calculation of the gravity–topography slope and geoid–topography ratio. (a) Anomalous swell topography contours (black lines) with a 0.25 km contour interval. Data were extracted every 20 km along 10 radial profiles (blue and red lines) diverging from the swell crest (red star). Long-wavelength spherical harmonic components of the satellite-derived gravity field (OSU91A, Pavlis & Rapp 1990) complete to degree and order $n = m \le 40$ (including anomalies with wavelengths greater than 1000 km), (b), and geoid (EGM96, Lemoine *et al.* 1998), (c), complete to degree and order $10 < n = m \le 40$ (including anomalies with wavelengths between 1000 and 4000 km). (d) Plot of gravity against topography, showing $1° \times 1°$ averages (black circles), individual profiles (blue and red lines) and the average of the four selected blue profiles (black line). The mean and standard deviation of the gravity–topography slope are 16.7 and 1.9 mGal km^{-1}, respectively. e) Plot of geoid against topography. The mean and standard deviation of the geoid–topography ratio are 3.77 and 0.38 m km^{-1}, respectively.

Substituting these values into eqs (2) and (3) produces estimates for the compensation depth of the swell of 55 ± 6 km and 77 ± 8 km, respectively. The expected lithospheric plate thickness is between 95 and 125 km, depending on the heat flow model used (95 km—Parsons & Sclater 1977; 125 km—Stein & Stein 1992) with an intermediate depth, based on a model incorporating the temperature dependence of thermal conductivity (McKenzie *et al.* 2005), of ∼105 km. This result can be interpreted in terms of two models:

(1) The compensation of the swell is entirely contained within the lithosphere as an anomalous region of low density extending to 60–80 km.

(2) There is a component of thermal compensation within the lithosphere with an additional component of dynamic upwelling impinging on the base of the lithosphere.

The second model is considered more likely given the observation of very long wavelength flexure that implies that the plate is regionally 'strengthened' by an upward-acting load.

9 DISCUSSION

The mechanisms that have been proposed to explain how the large-scale topographic swells associated with hotspot volcanism are sustained over geological timescales can be summarized as:

(1) Shallow support within the crust (e.g. Morgan *et al.* 1995), including hotspot-thickened crust,

(2) Support within the upper (lithospheric) mantle (e.g. Detrick & Crough 1978; Robinson 1988), and

(3) Dynamic mantle upwelling (e.g. Sleep 1995).

It is possible that these mechanisms are entirely independent or work in combination to produce the observed large-scale topographic anomalies. The Cape Verde Swell was identified as the ideal location to conduct an investigation into the relative contribution of these different support mechanisms due to its large size and geophysical characteristics.

Flexural modelling using the *final* velocity–depth model to constrain the crust, and its velocities to convert TWTT measurements of the sediment-basement surface and to calculate the moat infill thickness, resulted in a contradiction whereby the plate surface appears less flexed than its age would predict ($T_e = 30$ km), while the volume and density of the island and infill loads derived from seismic observations produce a gravity anomaly that matches the observed. The 'preferred' flexural model suggests a T_e of 60 km, and leads to the conclusion that the plate merely appears to be stronger than its age would suggest, due to an upward-acting unbending force. A body of low density at the base of, or beneath, the crust could provide an upward-acting force.

Ito & Clift (1998) suggested that the extent of undercrustal magmatic material at oceanic plateaus and oceanic islands may depend on the residence time of the hotspot, and that large bodies take >30 Ma to form. If this hypothesis is correct, then given that the Cape Verde Swell is thought to have formed between 40 and 20 Ma and that there has been little movement (~215 km, ENE) of the African Plate in this region in the last 30 Ma (Pollitz 1991), a significant body of undercrustal material should have accumulated.

Although the depth of the Moho increases from 12.5 to 13.5 km b.s.l., our *final* velocity–depth model (Fig. 2b), shows no evidence for a thicker than average lower crust along the entirety of profile P01. There is also no evidence for a lower crustal region of anomalously low velocity/density >2 km thick and >100 km wide similar to that at Hawaii (Watts & ten Brink 1989), Marquesas (Caress *et al.* 1995), La Réunion (Charvis *et al.* 1999), Ninetyeast Ridge (Grevemeyer *et al.* 2001) and Josephine Seamount (Peirce & Barton 1991). Instead, the slight curvature of the Moho is interpreted as a small downward deflection of the oceanic crust in response to surface loading.

Despite this lack of evidence, as part of 3-D flexure modelling, a series of models was tested to consider the possibility of an undercrustal load as the origin of the apparent upward-acting unbending force. These models incorporated varying amounts of positively buoyant undercrustal load to counteract the excess flexure caused by the surface loads. The observed thickness of moat infill sediments was closely matched using an undercrustal load with sub-Moho thickness of up to 2.0 km directly beneath the F-STR. Such a model was discounted as the crustal thickness exceeds that observed along profile P01 and that modelled directly beneath the islands from receiver function analyses (Lodge & Helffrich 2006).

The WA seismic data suggest that if undercrustal material is present at the Cape Verde archipelago it is entirely localized beneath the islands. Calculations also demonstrate that it would not provide sufficient buoyancy to fully support the islands, and certainly would have a negligible contribution to the regional topographic swell. Instead, any unbending force must originate deeper (beyond WA seismic imaging depths) either within the lithosphere, at the lithosphere–asthenosphere boundary, in the asthenosphere or as a combination of these.

Before investigating a deeper origin, multicomponent models with varying T_e were considered as a means of explaining the contradiction in T_e derived from solely the flexural surface ($T_e = 60$ km) and gravity anomaly ($T_e = 30$ km) fits. A variable T_e model incorporating 30 per cent of the total flexure associated with a T_e of 30 km and 70 per cent of the total flexure associated with a T_e of 60 km (Fig. 10c) generated the best-fit to the observed moat infill sediment thickness/sediment-basement surface geometry proximal to the island loads.

However, the residual gravity anomaly from the variable T_e model (Fig. 8f) is dominated by a negative anomaly ~350 km in diameter with an amplitude of up to −40 mGal. It is possible to estimate the size, shape and density contrast of a low-density body in the lithospheric mantle that would be required to reconcile the residual negative gravity anomaly. Several basic shapes have been considered by Wilson (2011) and Wilson *et al.* (2010), including an infinite horizontal slab, a buried sphere and a vertical cylinder, because they best represent the likely shape of a mantle-based, low-density region caused by melting or thermal rejuvenation. Assuming that the anomalous body has a shape intermediate between an infinite slab and a sphere, biased towards that of a vertical cylinder, the density contrast of the anomalous low-density region in the lithosphere required to fit the observed gravity anomaly is estimated to be -25 ± 10 kg m^{-3}, which would equate to a thermal anomaly of ~250 °C.

At the Canary Islands, where there is evidence of a topographic swell of amplitude ~1.5 km (Monnereau & Cazenave 1990; Crosby & McKenzie 2009), results from 3-D flexure modelling imply that the lithosphere is weaker than expected for its predicted thermal age (Watts *et al.* 1997). A coherence analysis of bathymetry and gravity data (Canales & Dañobeitia 1998) revealed a compensation depth of 40–65 km with a small negative density contrast of ~33 kg m^{-3} in the lithosphere, corresponding to an increased temperature of ~325 °C. Canales & Dañobeitia (1998) advocate the model of Robinson & Parsons (1988), which involves a low viscosity region in the uppermost asthenosphere reheating the lower lithosphere without affecting the thermal structure of the upper lithosphere; thereby the plate retains most of its age-predicted mechanical strength.

The density contrast invoked for the Canary Swell is similar in magnitude to that postulated here to account for the negative gravity anomaly observed. However, there is no evidence for thermal rejuvenation and weakening of the lithospheric plate at the Cape Verdes. It is, thus, possible that a combination of localized weakening and regional apparent strengthening still results in the observation of a plate that is generally stronger than expected based on its age.

A lack of evidence for a significant body of undercrustal material and less uplift than would be expected if it is associated with thermal rejuvenation, implies that dynamic mantle upwelling most likely plays the dominant role in supporting the regional swell. In this model, positively buoyant material rises through the asthenospheric mantle until it reaches the base of the lithosphere (e.g. Ribe & Christensen 1994). At this point, the upwelling column exerts an upward-acting load on the base of lithosphere and, if there is a low degree of thermal rejuvenation, the lithosphere retains its long-term strength and flexural deformation associated with this upward-acting load is transferred to the surface. In simple terms, the downward flexure associated with surface loading is unbent by an upward-acting buoyancy force that supports the swell.

McNutt (1988) calculates, using forward filtering and admittance techniques, that the depth of compensation for the bathymetric anomaly of the Cape Verde Swell is 69 ± 10 km. This result is in close agreement with the estimates obtained here (55 ± 6 and 77 ± 8 km) where forward filtering and linear regression techniques were used to determine the gravity–topography slope and the geoid–topography ratio, respectively. Consequently, the compensation depth is located within the lower lithosphere suggesting instead, that there may be a dual compensation mechanism involving a thermally induced region of low density within the lithosphere,

at an average depth of 50 km below the surface, coupled with an upward-acting dynamic load impinging on the base of the lithosphere at ∼100 km depth.

The dimensions of the low-density region beneath Hawaii are similar to that beneath the Cape Verde, allowing a direct comparison to be made (Montelli *et al.* 2006). Geodynamic modelling of thermal upwelling beneath a moving lithosphere was conducted by Ribe & Christensen (1994) to determine the buoyancy flux necessary to produce the amplitude of uplift observed at the Hawaiian Swell. The best-fitting model required the temperature of the upwelling column (180 km in diameter) to be 300 °C hotter than that of the surrounding mantle. In this model, the topography associated with thermal rejuvenation of the lithosphere, determined from uplift of isotherms, did not produce significant swell topography (less than half of that produced from pure dynamic upwelling).

Relative to the underlying asthenospheric mantle, the Pacific Plate in the region of the Hawaiian Islands moves roughly an order of magnitude faster than the African Plate in the region of the Cape Verde Islands (e.g. Gripp & Gordon 2002). Assuming a similar buoyancy flux for a dynamic upwelling beneath the Cape Verde region, which is reasonable given the comparable tomographic observations of Montelli *et al.* (2006), this would produce a topographic swell with a height of ∼1.0 km. The remaining anomalous topography could be produced by thermal rejuvenation of the lithosphere, which is also plausible given that the African Plate has remained almost stationary for at least 30 Myr (Pollitz 1991). This conclusion is supported by observations of positive heat flow anomalies (Fig. 1) that Courtney & White (1986) determine could produce up to 50 per cent of the total swell height.

In summary, the results of 3-D flexure modelling indicate that the lithospheric plate responds to surface loading with a mechanical strength greater than would be expected based on its age alone. To counteract the surface load, an upward-acting load must be present either within or below the lithosphere. There is no evidence to suggest the presence of an undercrustal body with sufficient buoyancy to support the loads of the islands let alone the entire swell, and analysis of the gravity–topography slope and the geoid–topography ratio implies that the swell is compensated at a depth of ∼70 km. This is towards the base of the lithospheric plate, ∼100 km, and suggests that dynamic upwelling impinging on the base of a rigid lithosphere may transfer regional uplift to the plate surface, and thermally rejuvenate the lower lithosphere due to the slow plate movement. Using receiver function analysis, Vinnik *et al.* (2012) provide supporting evidence for a low-density region in the lower lithospheric mantle (∼60–100 km), and they interpret such a layer as representing the residuum following basaltic melt extraction.

Other large mid-plate swells that are not linked to individual island groups or chains include the African Superswell (Nyblade & Robinson 1994) and the South Pacific Superswell (McNutt & Fischer 1987). The explanations provided for the mechanism(s) that supports the anomalous topography of these superswells (e.g. McNutt 1998) are equally contentious, with evidence for both thermal rejuvenation of the lithosphere (e.g. Nyblade & Robinson 1994) and dynamic upwelling in the asthenosphere (e.g. Adam & Bonneville 2005; Tanaka *et al.* 2009). Given that a thermal origin is often invoked for the buoyancy that drives the observed columnar asthenospheric upwelling, it becomes apparent that in areas where absolute plate motion is slow, anomalous swell height should initially be supported dynamically and that, over time, support from thermal rejuvenation should also contribute. Conversely, where absolute plate motion over a fixed asthenospheric source is rapid, support should be almost entirely dynamic.

A combined synthesis of the results reveals that the Cape Verde Swell is almost certainly supported by a combination of mechanisms. The evidence for shallow crustal support is, however, weak but cannot be entirely discounted. Dynamic support is thus invoked to explain the apparent regional strength of the lithosphere, which greatly exceeds that predicted from the standard plate-cooling model. Thermal rejuvenation may also occur beneath the archipelago, although the evidence for this is indirect given that flexure modelling shows that the plate is not weakened beyond its expected strength. Thus, any support from thermal rejuvenation must act in conjunction with regional dynamic support, which adds 'strength' to the plate.

10 CONCLUSIONS

The main conclusions that can be drawn from this study are as follows:

(1) From both forward and inverse modelling of the WA seismic data, no evidence was found for widespread thickened crust or lower crustal velocities exceeding 7.3 km s^{-1}, indicative of undercrustal magmatic material, beneath the Cape Verde region.

(2) Flexure modelling implies that the lithosphere is stronger than expected from its magnetic anomaly-derived age. Regional 'strengthening' and swell support by undercrustal loads is excluded by the seismic data and, instead, a model of dynamic upwelling within the asthenosphere is invoked which supports the swell topography and unbends a component of the load-induced plate flexure giving the appearance of a plate that is much stronger than would be expected for its age.

(3) A low-density region ($\Delta\rho$ −25 ±10 kg m^{-3}) in the lower lithosphere can reconcile the intermediate wavelength negative residual gravity anomaly that is observed after subtraction of the gravity effect of the best-fitting flexure model from the gravity anomaly, once the long wavelength swell has been removed.

(4) Analysis of the long-wavelength gravity–topography slope and geoid–topography ratio indicates a compensation depth for the swell of ∼70 km. This depth is within the lower lithosphere and may represent the combination of buoyancy support from within the lithosphere provided by the low-density region, and dynamic support from upwelling material impinging on the base of the lithosphere.

(5) The observed topographic swell, most likely, results from a column of hot upwelling material impinging on the base of the lithosphere, with conductive reheating a consequence of slow plate movement. This upwelling column produces the observed anomalous topography, gravity and geoid anomalies through a combination of dynamic support and thermal rejuvenation of the lithosphere.

(6) There is no evidence that thermal rejuvenation has significantly weakened the lithosphere. To the contrary, the results of both seismic and flexure modelling are compatible with a model in which the Cape Verde Islands were emplaced on normal strength lithosphere that was being deformed from below by hot upwelling mantle, a process that began in the Neogene and may still be continuing today.

officers and crew of the 'R/V Meteor' and the sea-going scientists for their efforts. Independent traveltime inversions were carried out at the IFM-GEOMAR ocean-bottom seismic data processing and modelling facility (project number: RITA-CT-2004-505322-2008/4). The GMT and Seismic Unix software packages (Wessel & Smith 1998 and Cohen & Stockwell 2000, respectively) were used to create the figures for this paper. Finally, we thank George Helffrich and an anonymous reviewer for their comments.

REFERENCES

Adam, C. & Bonneville, A., 2005. Extent of the South Pacific Superswell, *J. geophys. Res.,* **110,** B09408, doi:10.1029/2004JB003465.

Ali, M.Y., Watts, A.B. & Hill, I., 2003. A seismic reflection profile study of lithospheric flexure in the vicinity of the Cape Verde Islands, *J. geophys. Res.,* **108,** 2239, doi:10.1029/2002JB002155.

Bowin, C., 1983. Depth of principle mass anomalies contribution to the Earth's geoidal undulations and gravity anomalies, *Mar. Geodesy,* **7,** 61–100.

Canales, J.P. & Dañobeitia, J.J., 1998. The Canary Islands swell: a coherence analysis of bathymetry and gravity, *Geophys. J. Int.,* **132,** 479–488.

Cande, S.C. & Kent, D.V., 1992. A new geomagnetic polarity time scale for the Late Cretaceous and Cenozoic, *J. geophys. Res.,* **97,** 13 917–13 951.

Cande, S.C. & Kent, D.V., 1995. Revised calibration of the geomagnetic polarity timescale, *J. geophys. Res.,* **100,** 6093–6095.

Caress, D.W., McNutt, M.K., Detrick, R.S. & Mutter, J.C., 1995. Seismic imaging of hotspot-related crustal underplating beneath the Marquesas Islands, *Nature,* **373,** 600–603.

Carlson, R.L. & Raskin, G.S., 1984. Density of the ocean crust, *Nature,* **311,** 555–558.

Cazenave, A., Dominh, K., Rabinowicz, M. & Ceuleneer, G., 1988. Geoid and depth anomalies over ocean swells and troughs: evidence of an increasing trend of the geoid to depth ratio with age of plate, *J. geophys. Res.,* **93,** 8064–8077.

Charvis, P. *et al.*, 1999. Spatial distribution of hotspot material added to the lithosphere under La Réunion, from wide-angle seismic data, *J. geophys. Res.,* **104,** 2875–2893.

Cochran, J.R., 1979. An analysis of isostasy in the world's oceans 2. Midocean ridge crests, *J. geophys. Res.,* **84,** 4713–4729.

Cohen, J. & Stockwell, J., 2000. *CWP/SU: Seismic Unix release 34: a free package for seismic research and processing,* Centre for Wave Phenomenon, Colorado School of Mines.

Courtney, R.C. & White, R.S., 1986. Anomalous heat flow and geoid across the Cape Verde Rise: evidence for dynamic support from a thermal plume in the mantle, *Geophys. J. R. astr. Soc.,* **87,** 815–867.

Crosby, A.G. & McKenzie, D., 2009. An analysis of young ocean depth, gravity and global residual topography, *Geophys. J. Int.,* **178,** 1198–1219.

Crosby, A.G., McKenzie, D. & Sclater, J.G., 2006. The relationship between depth, age and gravity in the oceans, *Geophys. J. Int.,* **166,** 553–573.

Crough, S.T., 1983. Hotspot swells, *Ann. Rev. Earth planet. Sci.,* **11,** 165–193.

Crough, S.T. & Jurdy, D.M., 1980. Subducted lithosphere, hotspots and the geoid, *Earth planet. Sci. Lett.,* **48,** 15–22.

Davis, E.E. & Lister, C.R.B., 1974. Fundamentals of ridge crest topography, *Earth planet. Sci. Lett.,* **21,** 405–413.

Day, S.J., da Silva, S.I.N.H. & Fonseca, J.F.B.D., 1999. A past giant lateral collapse and present-day flank instability of Fogo, Cape Verde Islands, *J. Volc. Geotherm. Res.,* **94,** 191–218.

Detrick, R.S. & Crough, S.T., 1978. Island subsidence, hot spots, and lithospheric thinning, *J. geophys. Res.,* **83,** 1236–1244.

Duncan, R.A. & Keller, R.A., 2004. Radiometric ages for basement rocks from the Emperor Seamounts, ODP Leg 197, *Geochem. Geophys. Geosyst.,* **5,** Q08L03, doi:10.1029/2004GC000704.

Duncan, R.A. & Richards, M.A., 1991. Hotspots, mantle plumes, flood basalts, and true polar wander, *Rev. Geophys.,* **29,** 31–50.

Duprat, H.I., Friis, J., Holm, P.M., Grandvuinet, T. & Sørensen, R.V., 2007.

The volcanic and geochemical development of São Nicolau, Cape Verde Islands: constraints from field and 40Ar/39Ar evidence, *J. Volc. Geotherm. Res.,* **162,** 1–19.

Dyhr, C.T. & Holm, P.M., 2010. A volcanological and geochemical investigation of Boa Vista, Cape Verde Islands; 40Ar/39Ar geochronology and field constraints, *J. Volc. Geotherm. Res.,* **189,** 19–32.

Grevemeyer, I., 1999. Isostatic geoid anomalies over mid-plate swells in the Central North Atlantic, *Geodynamics,* **28,** 41–50.

Grevemeyer, I. & The Shipboard Scientific Party, 2004. Meteor report, Equatorial and South Atlantic, Part 3, Cruise no. M62, Leg 3, CHARISMA—Cape Verde Hotspot: A Seismic Refraction study of ISostasy and MAgmatic underplating. Cruise report (unpublished), IFM-GEOMAR.

Grevemeyer, I., Flueh, E.R., Reichert, C., Bialas, J., Klaschen, D. & Kopp, C., 2001. Crustal architecture and deep structure of the Ninetyeast Ridge hotspot trail from active-source ocean bottom seismology, *Geophys. J. Int.,* **144,** 414–431.

Gripp, A.E. & Gordon, R.G., 2002. Young tracks of hotspot and current plate velocities, *Geophys. J. Int.,* **150,** 321–361.

Hamilton, E.L., 1978. Sound velocity-density relations in sea-floor sediments and rocks, *J. acoust. Soc. Am.,* **63,** 366–377.

Haxby, W.F. & Turcotte, D.L., 1978. On isostatic geoid anomalies, *J. geophys. Res.,* **83,** 5473–5478.

Hayes, D.E., 1988. Age-depth relationships and depth anomalies in the southeast Indian Ocean and south Atlantic Ocean, *J. geophys. Res.,* **93,** 2937–2954.

Hayes, D.E. & Rabinowitz, P.D., 1975. Mesozoic magnetic lineations and the magnetic quiet zone off northwest Africa, *Earth planet. Sci. Lett.,* **28,** 105–115.

Holm, P.M., Grandvuinet, T., Friis, J., Wilson, J.R., Barker, A.K. & Plesner, S., 2008. An 40Ar/39Ar study of the Cape Verde hot spot: temporal evolution in a semistationary plate environment, *J. geophys. Res.,* **113,** B08201, doi:10.1029/2007JB005339.

IOC, IHO & BODC, 2003. Centenary Edition of the GEBCO Digital Atlas, published on CD-ROM on behalf of the Intergovernmental Oceanographic Commission and the International Hydrographic Organisation as part of the General Bathymetric Chart of the Oceans, British Oceanographic Data Centre, Liverpool.

Ito, G. & Clift, P.D., 1998. Subsidence and growth of Pacific Cretaceous plateaus, *Earth planet. Sci. Lett.,* **161,** 85–100.

Kalnins, L.M. & Watts, A.B., 2009. Spatial variations in effective elastic thickness in the western Pacific Ocean and their implications for Mesozoic volcanism, *Earth planet. Sci. Lett.,* **286,** 89–100.

Kim, S.-S. & Wessel, P., 2008. Directional median filtering for regional-residual separation of bathymetry, *Geochem. Geophys. Geosys.,* **9,** Q03005, doi:10.1029/2007GC001850.

Koppers, A.A.P., Duncan, R.A. & Steinberger, B., 2004. Implications of a nonlinear 40Ar/39Ar age progression along the Louisville seamount trail for models of fixed and moving hot spots, *Geochem. Geophys. Geosyst.,* **5,** Q06L02, doi:10.1029/2003GC000671.

Korenaga, J., Holbrook, W.S., Kent, G.M., Kelemen, P.B., Detrick, R.S., Larsen, H.C., Hopper, J.R. & Dahl-Jensen, T., 2000. Crustal structure of the southeast Greenland margin from joint refraction and reflection seismic tomography, *J. geophys. Res.,* **105,** 21 591–21 614.

LaBrecque, J.L., Kent, D.V. & Cande, S.C., 1977. Revised magnetic polarity time scale for Late Cretaceous and Cenozoic time, *Geology,* **5,** 330–335.

Lancelot, Y. & The Shipboard Scientific Party, 1978a. Site 367: Cape Verde Basin, in *Init. Rep. DSDP,* Vol. 41, pp. 163–232, eds Lancelot, Y., Seibold, E. & Gardner, J.V., US Government Printing Office, Washington, DC.

Lancelot, Y. & The Shipboard Scientific Party, 1978b. Site 368: Cape Verde Rise, in *Init. Rep. DSDP,* Vol. 41, pp. 233–326, eds Lancelot, Y., Seibold, E. & Gardner, J.V., US Government Printing Office, Washington, DC.

Lemoine, F.G. *et al.*, 1998. The development of the joint NASA, GSFC and the National Imagery and Mapping Agency (NIMA) geopotential model EGM96. NASA Technical Report, NASA/TP-1998-206861.

Lodge, A. & Helffrich, G., 2006. Depleted swell root beneath the Cape Verde Islands, *Geology,* **34,** 449–452.

Madeira, J., Mata, J., Mourão, C., da Silveira, A.B., Martins, S., Ramalho, R. & Hoffmann, D.L., 2010. Volcano-stratigraphic and structural

evolution of Brava Island (Cape Verde) based on 40Ar/39Ar, U-Th and field constraints, *J. Volc. Geotherm. Res.,* **196,** 219–235.

Marks, K.M. & Sandwell, D.T., 1991. Analysis of geoid height versus topography for oceanic plateaus and swells using nonbiased linear regression, *J. geophys. Res.,* **96,** 8045–8055.

Marks, K.M. & Smith, W.H.F., 2007. Some remarks on resolving seamounts in satellite gravity, *Geophys. Res. Lett.,* **34,** L03307, doi:10.1029/2006GL028857.

Marty, J.C. & Cazenave, A., 1989. Regional variations in subsidence rate of oceanic plates: a global analysis, *Earth planet. Sci. Lett.,* **94,** 301–315.

Masson, D.G., Le Bas, T.P., Grevemeyer, I. & Weinrebe, W., 2008. Flank collapse and large-scale landsliding in the Cape Verde Islands, off West Africa, *Geochem. Geophys. Geosyst.,* **9,** Q07015, doi:10.1029/2008GC001983.

McKenzie, D., Jackson, J. & Priestley, K., 2005. Thermal structure of oceanic and continental lithosphere, *Earth planet. Sci. Lett.,* **233,** 337–349.

McNutt, M., 1988. Thermal and mechanical properties of the Cape Verde Rise, *J. geophys. Res.,* **93,** 2784–2794.

McNutt, M.K., 1998. Superswells, *Rev. Geophys.,* **36,** 211–244.

McNutt, M. & Fischer, K., 1987. The South Pacific Superswell, in *Seamounts, Islands, and Atolls,* Geophys. Monogr. Ser., Vol. 43, pp. 25–34, eds Keating, B.H., Fryer, P., Batiza, R. & Boehlert, G.W., AGU, Washington, DC.

Mitchell, J.G., Le Bas, M.J., Zielonka, J. & Furnes, H., 1983. On dating the magmatism of Maio, Cape Verde Islands, *Earth planet. Sci. Lett.,* **64,** 61–76.

Monnereau, M. & Cazenave, A., 1990. Depth and geoid anomalies over oceanic hotspot swells: a global survey, *J. geophys. Res.,* **95,** 15 429–15 438.

Monnereau, M., Rabinowicz, M. & Arquis, E., 1993. Mechanical erosion and reheating of the lithosphere: a numerical model for hotspot swells, *J. geophys. Res.,* **98,** 809–823.

Montelli, R., Nolet, G., Dahlen, F.A. & Masters, G., 2006. A catalogue of deep mantle plumes: new results from finite-frequency tomography, *Geochem. Geophys. Geosys.,* **7,** Q11007, doi:10.1029/2006GC001248.

Morgan, W.J., 1983. Hotspot tracks and the early rifting of the Atlantic, *Tectonophysics,* **94,** 123–139.

Morgan, J.P., Morgan, W.J. & Price, E., 1995. Hotspot melting generates both hotspot volcanism and a hotspot swell? *J. geophys. Res.,* **100,** 8045–8062.

Müller, R.D., Roest, W.R., Royer, J.Y., Gahagan, L.M. & Sclater, J.G., 1997. Digital isochrons of the world's ocean floor, *J. geophys. Res.,* **102,** 3211–3214.

Müller, R.D., Sdrolias, M., Gaina, C. & Roest, W.R., 2008. Age, spreading, and spreading asymmetry of the world's ocean crust, *Geochem. Geophys. Geosys.,* **9,** Q04006, doi:10.1029/2007GC001743.

Nyblade, A.A. & Robinson, S.W., 1994. The African Superswell, *Geophys. Res. Lett.,* **21,** 765–768.

Parker, R.L., 1972. The rapid calculation of potential anomalies, *Geophys. J. R. astr. Soc.,* **31,** 447–455.

Parsons, B. & Sclater, J.G., 1977. An analysis of the variation of ocean floor bathymetry and heat flow with age, *J. geophys. Res.,* **82,** 803–827.

Pavlis, N.K. & Rapp, R.H., 1990. The development of an isostatic gravitational model to degree and order 360 and its use in global gravity modelling, *Geophys. J. Int.,* **100,** 369–378.

Peirce, C. & Barton, P.J., 1991. Crustal structure of the Madeira-Tore Rise, eastern North Atlantic—results of a DOBS wide-angle and normal incidence seismic experiment in the Josephine Seamount region, *Geophys. J. Int.,* **106,** 357–378.

Pim, J., Peirce, C., Watts, A.B., Grevemeyer, I. & Krabbenhoeft, A., 2008. Crustal structure and origin of the Cape Verde Rise, *Earth planet. Sci. Lett.,* **272,** 422–428.

Plesner, S., Holm, P.M. & Wilson, J.R., 2003. 40Ar/39Ar geochronology of Santo Antão, Cape Verde Islands, *J. Volc. Geotherm. Res.,* **120,** 103–121.

Pollack, H.N., Hurter, S.J & Johnson, J.R., 1993. Heat flow from the Earth's interior: analysis of the global data set, *Rev. Geophys.,* **31,** 267–280.

Pollitz, F.F., 1991. Two-stage model of African absolute motion during the last 30 million years, *Tectonophysics,* **194,** 91–106.

Ramalho, R., Helffrich, G., Cosca, M., Vance, D., Hoffmann, D. & Schmidt, D.N., 2010. Episodic swell growth inferred from variable uplift of the Cape Verde hotspot islands, *Nature Geosci. Lett.,* **3**(11), 774–777.

Rees, B.A., Detrick, R.S. & Coakley, B.J., 1993. Seismic stratigraphy of the Hawaiian flexural moat, *Bull. geol. Soc. Am.,* **105,** 189–205.

Ribe, N.M. & Christensen, U.R., 1994. Three-dimensional modeling of plume-lithosphere interaction, *J. geophys. Res.,* **99,** 669–682.

Robinson, E.M., 1988. The topographic and gravitational expression of density anomalies due to melt extraction in the uppermost oceanic mantle, *Earth planet. Sci. Lett.,* **90,** 221–228.

Robinson, E.M. & Parsons, B., 1988. Effect of shallow low-viscosity zone on the formation of midplate swells, *J. geophys. Res.,* **93,** 3144–3156.

Sandwell, D.T. & MacKenzie, K.R., 1989. Geoid height versus topography for oceanic plateaus and swells, *J. geophys. Res.,* **94,** 7403–7418.

Sandwell, D.T. & Smith, W.H.F., 1997. Marine gravity anomaly from Geosat and ERS 1 satellite altimetry, *J. geophys. Res.,* **102,** 10 039–10 054.

Sandwell, D.T. & Smith, W.H.F., 2009. Global marine gravity from retracked Geosat and ERS-1 altimetry: ridge segmentation versus spreading rate, *J. geophys. Res.,* **114,** B01411, doi:10.1029/2008JB006008.

Sclater, J.G., Jaupart, C. & Galson, D., 1980. The heat flow through oceanic crust and continental crust and the heat loss of the Earth, *Rev. Geophys. Space Phys.,* **18,** 269–311.

Sleep, N.H., 1995. Geophysics—a wayward plume, *Nature,* **378,** 19–20.

Stein, C.A. & Stein, S., 1992. A model for the global variation in oceanic depth and heat flow with lithospheric age, *Nature,* **359,** 123–129.

Stillman, C.J., Furnes, H., Lebas, M.J., Robertson, A.H.F. & Zielonka, J., 1982. The geological history of Maio, Cape Verde Islands, *J. geol. Soc.,* **139,** 347–361.

Tanaka, S. *et al.*, 2009. P-wave tomography of the mantle beneath the South Pacific Superswell revealed by joint ocean floor and islands broadband seismic experiments, *Phys. Earth. planet. Inter,* **172,** 268–277.

Vinnik, L., Silveira, G., Kiselev, S., Farra, V., Weber, M. & Stutzmann, E., 2012. Cape Verde hotspot from the upper crust to the top of the lower mantle, *Earth planet. Sci. Lett.,* **319–320,** 259–268.

Walcott, R.I., 1976. Lithospheric flexure, analysis of gravity anomalies, and the propagation of seamount chains, in *The Geophysics of the Pacific Ocean Basin and Its Margins,* pp. 431–438, eds Sutton, G.H., Manghnani, M.H. & Moberly, R., American Geophysical Union, Washington, DC.

Watts, A.B., 1976. Gravity and bathymetry in the central Pacific Ocean, *J. geophys. Res.,* **81,** 1533–1553.

Watts, A.B., 1978. An analysis of isostasy in the world's oceans: 1. Hawaiian-Emperor seamount chain, *J. geophys. Res.,* **83,** 5989–6004.

Watts, A.B., 2001. *Isostasy and Flexure of the Lithosphere,* Cambridge University Press, Cambridge.

Watts, A.B. & ten Brink, U.S., 1989. Crustal structure, flexure, and subsidence history of the Hawaiian Islands, *J. geophys. Res.,* **94,** 10 473–10 500.

Watts, A.B. & Burov, E.B., 2003. Lithospheric strength and its relationship to the elastic and seismogenic layer thicknesses, *Earth planet. Sci. Lett.,* **213,** 113–131.

Watts, A.B. & Zhong, S., 2000. Observations of flexure and the rheology of oceanic lithosphere, *Geophys. J. Int.,* **142,** 855–875.

Watts, A.B., Peirce, C., Collier, J., Dalwood, R., Canales, J.P. & Henstock, T.J., 1997. A seismic study of lithospheric flexure in the vicinity of Tenerife, Canary Islands, *Earth planet. Sci. Lett.,* **146,** 431–447.

Watts, A.B., Sandwell, D.T., Smith, W.H.F. & Wessel, P. 2006. Global gravity, bathymetry, and the distribution of submarine volcanism through space and time, *J. geophys. Res.,* **111,** B08408, doi:10.1029/2005JB004083.

Wessel, P. & Smith, W.H.F., 1998. New improved version of the Generic Mapping Tools released, *EOS, Trans. Am. geophys. Un.,* **79,** 579.

White, R.S., McKenzie, D. & Onions, R.K., 1992. Oceanic crustal thickness from seismic measurements and rare-earth element inversions, *J. geophys. Res.,* **97,** 19 683–19 715.

Williams, C.A., Hill, I.A., Young, R. & White, R.S., 1990. Fracture zones across the Cape Verde Rise, NE Atlantic, *J. Geol. Soc.,* **147,** 851–857.

Wilson, D.J., 2011. Crustal structure of the Cape Verde Swell: insights into the flexural response of the lithosphere to loading, *PhD thesis,* Durham University, Durham, UK, 259pp.

Wilson, D.J., Peirce, C., Watts, A.B., Grevemeyer, I. & Krabbenhoeft, A., 2010. Uplift at lithospheric swells—I: seismic and gravity constraints on the crust and uppermost mantle structure of the Cape Verde mid-plate swell, *Geophys. J. Int.,* **182,** 531–550.

Wilson, J.T., 1963. Evidence from islands on spreading of ocean floors, *Nature,* **197,** 536–538.

Zelt, C.A., 1998. Lateral velocity resolution from three-dimensional seismic refraction data, *Geophys. J. Int.,* **135,** 1101–1112.

Zelt, C.A. & Barton, P.J., 1998. Three-dimensional seismic refraction to-mography: a comparison of two methods applied to data from the Faeroe Basin, *J. geophys. Res.,* **103,** 7187–7210.

Zelt, C.A. & Smith, R.B., 1992. Seismic traveltime inversion for 2-D crustal velocity structure, *Geophys. J. Int.,* **108,** 16–34.

Zheng, Y. & Arkani-Hamed, J., 2002. Rigidity of the Atlantic oceanic lithosphere beneath New England seamounts. *Tectonophysics,* **359,** 359–369.